Mantle sources underlying Nyiragongo volcano

DOI:
10.1016/j.chemgeo.2024.122607

Document Version
Accepted author manuscript

Citation for published version (APA):
Molendijk, S., Namur, O., & Neave, D. A. (2025). Mantle sources underlying Nyiragongo volcano. *Chemical Geology*, *675*, Article 122607. https://doi.org/10.1016/j.chemgeo.2024.122607

Published in:
Chemical Geology

Mantle sources underlying Nyiragongo volcano

Sander Molendijk[1,2*], Olivier Namur[1], David A. Neave[3]

[1] Department of Earth and Environmental Sciences, KU Leuven, Celestijnenlaan 200E, 3001 Leuven, Belgium

[2] Département de Géologie, Université de Liège, B-4000 Liège, Belgium

[3] Department of Earth and Environmental Sciences, The University of Manchester, Oxford Road, Manchester, M13 9PL, United Kingdom

(*Corresponding Author: s.m.molendijk@gmail.com)

Abstract

The Nyiragongo volcano, part of the Virunga Volcanic Province (VVP) in the Democratic Republic of Congo is a uniquely silica-undersaturated (32 – 49 wt.% SiO_2) and alkali-rich (7 – 17 wt.% $Na_2O + K_2O$) volcanic system. Though alkaline volcanism is by no means rare in the western branch of the East African Rift System (EARS), compositions erupted by Nyiragongo are nevertheless notably alkaline, especially given that the other volcanoes in the VVP predominantly erupt silica-saturated compositions. In order to address the origin of the geochemical character of Nyiragongo it is imperative to understand the mantle source feeding its plumbing system. We approach this issue through the combined analysis of primitive whole-rock samples and early-crystallized olivine hosted by these samples. Major and trace element compositional data from olivine indicates a Ca-rich, but otherwise unremarkable geochemical signature indicative of melt derivation from a peridotite restite. However, whole-rock compositions require melting of a K-rich phlogopite bearing source in the presence of apatite, garnet, and clinopyroxene to produce Si-undersaturated, Ca-, and K- rich melts. Geochemical modelling using recently acquired partition coefficients suggests that such melting must occur primarily at high pressures (~ 3 GPa), outside of the stability field of amphibole, in line with Nyiragongo residing on thick lithosphere bordering the Tanzanian craton.

Combining the peridotite restite-signature from olivine compositions with the phlogopite-pyroxenite melt-source inferred from whole-rock data results in a model of metasomatic vein-melting, wherein veins emplaced in the subcontinental lithospheric mantle during the Pan-African orogeny are preferentially molten through a breakdown reaction of phlogopite at

temperatures of 1150 to 1350 °C. These melts subsequently equilibrate with the surrounding peridotite mantle, resulting in a peridotite-restite signature observed in olivine.

Keywords: Nyiragongo; olivine trace elements; phlogopite; alkaline magmas; mantle source

1. INTRODUCTION

Volcanic activity in continental rift zones produces a large variety of exotic, often silica-undersaturated magma compositions (e.g., Sahama, 1962; Bell and Powell, 1969; Freestone and Hamilton, 1980; Moore and Kyle, 1987; Peterson, 1990; Caldwell and Kyle, 1994; Eby *et al.*, 2003; Keller *et al.*, 2006; Klaudius and Keller, 2006; Muravyeva *et al.*, 2021), attributed to a combination of small-degree mantle melting (e.g., Bultitude and Green, 1971; Altherr *et al.*, 1988; Haase *et al.*, 2000; Fitton, 2008; Martin *et al.*, 2010) and lithospheric erosion driven melting of the subcontinental lithospheric mantle (SCLM; Bedini *et al.*, 1997; Furman and Graham, 1999; Pilet *et al.*, 2008; Chakrabarti *et al.*, 2009a; Furman *et al.*, 2015; Heinonen *et al.*, 2016; Mollex *et al.*, 2018; Pitcavage *et al.*, 2021, 2023). The East African Rift System (EARS) has ample examples of this phenomenon, being a far-stretching active continental rift zone (Furman and Graham, 1999; Furman *et al.*, 2006, 2015; Pouclet *et al.*, 2016; Nelson *et al.*, 2019). Mantle heterogeneity is one of the most important factors influencing the high variety of igneous activity in the EARS (Foley *et al.*, 2012), producing both large-scale chemical trends (e.g., between western and eastern rift, see section 2.1) and small-scale anomalies like carbonatite and kamafugite volcanism (Aiuppa *et al.*, 2021; Innocenzi *et al.*, 2024). As such, understanding the mantle sources and melting conditions in this region is essential for attaining a broader understanding of the ways in which compositionally rare melts are generated. In addition, developing a better view of the mantle domains underlying the EARS is essential to modelling global geochemical reservoirs accurately and may help us to better understand the processes impacting and influencing the upper mantle.

One region of the EARS influenced by an anomalous, yet thus far incompletely understood mantle is the Virunga Volcanic Province (VVP), located where the borders of Rwanda, Uganda, and the Democratic Republic of Congo meet. This volcanic province contains eight volcanic edifices and numerous pyroclastic cones (Fig. 1b) which erupt a highly compositionally variable array of volcanic products (e.g., Barette *et al.*, 2017). Indeed, a laterally, and potentially vertically

heterogeneous mantle source has been repeatedly argued for in this region in order to explain compositional differences from foidites (Nyiragongo) to trachytes (Karasimbi) over the span of tens of kilometres (Vollmer and Norry, 1983a; Furman and Graham, 1999; Chakrabarti *et al.*, 2009a; Minissale *et al.*, 2022; Pitcavage *et al.*, 2023). Investigations into the high chemical variability observed between volcanoes in the VVP have repeatedly indicated that the primary magmatic liquids have a strong control on the chemical profile of each volcano (Marcelot and Rançon, 1988; Toscani *et al.*, 1990; Platz *et al.*, 2004; Condomines *et al.*, 2015; Molendijk *et al.*, 2024). For this reason, the current study attempts use the chemical signatures of the most primitive lavas and olivine crystals found at the Nyiragongo volcano, the most chemically extreme system in the VVP, to identify the mantle source underlying it. In addition, this study presents crystallization temperature estimates of olivine – chromite pairs in an attempt to infer the thermal state of this mantle source.

2. PREVIOUS WORK

2.1. VVP mantle sources

The EARS is separated into a western and an eastern branch (Fig. 1a), both of which coincide with the margins of the deep-rooted and mechanically strong Archaean Tanzanian craton (McConnel, 1972; Ebinger, 1989; Ebinger and Sleep, 1998; Chorowicz, 2005; Stamps *et al.*, 2008). Though some lines of evidence point towards volcanic activity in the western rift as early as 26 Ma (Roberts *et al.*, 2012), this branch is generally thought to have formed around 12 – 10 Ma, due to stress transmission from the main eastern branch through the craton (Nyblade and Brazier, 2002). The separation coincided with volcanic activity in this region which moved southward from the VVP (11 Ma) and South Kivu (10 Ma) to Rungwe (9 Ma) (Ebinger and Furman, 2003; Fontijn *et al.*, 2012; Roberts *et al.*, 2012). Volcanic activity in the western branch of the EARS is smaller in scale and more K-rich than what is erupted in the eastern branch, and is generally assumed to be at least indirectly related to plume activity (Ebinger and Furman, 2003).

Whereas lavas from the VVP itself have no clear elevated $^{3}He/^{4}He$ ratios suggestive of a deep mantle origin (Pik *et al.*, 2006), there exists convincing geochemical (Dawson *et al.*, 1994; Hilton *et al.*, 2011; Halldórsson *et al.*, 2014) and tomographical (Grijalva *et al.*, 2018; Njinju *et al.*, 2021) evidence for a plume source under Rungwe. It has been argued that volcanism further north may

be the result of mixing between this plume source and SCLM material, diluting the He-isotope plume signature (Halldórsson *et al.*, 2014). Regardless of whether the source underlying the VVP is plume-related (Chakrabarti *et al.*, 2009a; Castillo *et al.*, 2014) or derived primarily from the SCLM (Furman and Graham, 1999; Muravyeva *et al.*, 2014; Pitcavage *et al.*, 2021, 2023; Minissale *et al.*, 2022), authors agree on the requirement of metasomatic influences in generating its heterogeneity. While some regions provide hints to their underlying mantle compositions through mantle xenoliths (Lloyd, 1981; Dawson and Smith, 1988, 1992; Rudnick *et al.*, 1993; Dawson *et al.*, 1995), no such samples are available for the VVP, meaning inferences about mantle assemblages in this region have primarily weighed on whole-rock geochemical data.

Vollmer and Norry (1983) first inferred metasomatism-driven heterogeneity from unusual isotope systematics in lavas from Nyiragongo, dating back to a metasomatic event at ~500 Ma. Metasomatic influences were corroborated by Williams and Gill (1992), also based on Th isotopes. Furman and Graham (1999) provided the first indications that the SCLM under the VVP must be an amphibole/phlogopite-bearing garnet peridotite locally affected by carbonate metasomatism. This type of mantle assemblage is similar to what has been suggested and more directly observed for other volcanic provinces surrounding the Tanzanian craton such as the Manyara-Balangida rift and Toro-Ankole (Koornneef *et al.*, 2009; Foley *et al.*, 2012; Baudouin and Parat, 2020; Pitcavage *et al.*, 2021; Innocenzi *et al.*, 2024).

Disagreements remain regarding amphibole, which Rosenthal *et al.* (2009) and Pitcavage *et al.* (2023) suggest is required to explain the sodic character of the rocks, whereas Chakrabarti *et al.* (2009) explicitly excludes the presence of amphibole in the Nyiragongo source based on low K/Rb ratios. No xenolith data are available from the region other than fused granitic rocks representing the Precambrian basement underlying the VVP (Sahama and Meyer, 1958; Sahama, 1978). Given the high trace-element content of the lavas of Nyiragongo (Hertogen *et al.*, 1985; Platz *et al.*, 2004; Molendijk *et al.*, 2024), as well as their silica-undersaturated character, contamination of this basement rock was repeatedly deemed minimal (Bell and Powell, 1969; Hertogen *et al.*, 1985; Chakrabarti *et al.*, 2009a).

2.2. Nyiragongo volcano

The Nyiragongo volcano is characterized by extremely alkali-rich (7 – 17 wt.% $Na_2O + K_2O$), silica-undersaturated (32 – 49 wt.% SiO_2) lavas, making it the most silica-undersaturated volcano in the VVP (Platz *et al.*, 2004; Barette *et al.*, 2017; Molendijk *et al.*, 2024), and one of the most alkaline volcanoes on Earth. The eruptive products of Nyiragongo can be split into primitive (olivine melilite basalts) and evolved (nephelinites, melilitites, leucitites) compositions, the former of which erupt from pyroclastic cones on the flanks of the volcano rather than the main cone (Fig. 1c; Demant *et al.*, 1994; Platz *et al.*, 2004; Molendijk *et al.*, 2024). The evolved lavas of Nyiragongo's main cone are feldspathoid-rich and frequently present glomeroporphyritic textures, resulting from synneusis and floatation of nepheline and leucite in the liquid-dominated lava lake that represents the final part of the plumbing system (Molendijk *et al.*, 2024). Fractionation modelling and observations of primitive enclaves within evolved lavas indicate that the main cone melts can be linked to those of the pyroclastic cones by fractional crystallization processes, with the pyroclastic cones sampling more primitive melts (Demant *et al.*, 1994; Platz *et al.*, 2004; Molendijk *et al.*, 2024). Most studies have inferred that the primary melt of Nyiragongo is most likely an olivine melilite basalt such as is erupted from the pyroclastic cones south-west of the main edifice (Demant *et al.*, 1994; Platz *et al.*, 2004; Molendijk *et al.*, 2024). However, attempts at fractionation modelling from such a melt composition indicates that the chemical signature of Nyiragongo is derived from the mantle source, rather than a unique fractional crystallization regime (Molendijk *et al.*, 2023, 2024). Recent studies on mantle sources in the VVP agree with the requirement of a carbonated, garnet- and phlogopite-rich peridotite mantle (Chakrabarti *et al.*, 2009a; Condomines *et al.*, 2015; Minissale *et al.*, 2022) underlying both Mugogo and Nyiragongo. These conclusions are largely built on whole-rock Pb, Nd, Sr, and Hf systematics (Vollmer and Norry, 1983a, 1983b; Chakrabarti *et al.*, 2009a; Muravyeva *et al.*, 2021; Pitcavage *et al.*, 2021) as well as Zr/Hf and Th/U ratios (Condomines *et al.*, 2015). Authors agree that the mantle lithology must have at least contained garnet and phlogopite, as evidenced by (1) high light rare earth element/heavy rare earth element (LREE/HREE) ratios, (2) low K/Rb ratios (< 231 – 356) (Chakrabarti *et al.*, 2009a), (3) high Th/U ratios, and (4) a Ra deficit (Condomines *et al.*, 2015). Carbonate metasomatism is additionally inferred through high Zr/Hf ratios (Dupuy *et al.*, 1992), though Condomines *et al.* (2015) argued that carbonatite melts may contain insufficient Zr and Hf to adequately affect these ratios.

All the estimates made for the VVP and Nyiragongo thus far have been qualitative in nature and fundamentally rest on whole-rock data that may easily be affected by assimilation-fractional crystallization (AFC) processes. However, mantle sources have increasingly been probed through the lens of olivine compositions, bypassing such effects (Sobolev *et al.*, 2005, 2007; Foley *et al.*, 2013; Neave *et al.*, 2018). For this reason, this study combines whole-rock analyses with major and trace element compositional data of primitive olivine crystals in order to further elucidate the most probable mantle source of Nyiragongo.

3. SAMPLING AND ANALYTICAL METHODS

3.1. Samples

This study presents measurements from olivine phenocrysts selected from some of the most olivine-rich lavas erupted by the Nyiragongo volcano, collected and discussed in detail by Molendijk *et al.* (2024). A subset of this dataset has already been published but will be discussed further here. In addition to this previously collected dataset we present new measurements from olivine derived from samples Ny17-142, Ny17-161, Ny17-163 (Table 1) of the same study, detailed descriptions of which can be found in Molendijk *et al.* (2024). All samples were collected during expeditions to the lava plain of Nyiragongo in 2017 and 2019 and are derived from the lavas emitted by the pyroclastic cones flanking the southern side of the Nyiragongo main cone (Fig. 1c). The samples concern basaltic lava flows with variable contents of clinopyroxene, melilite, and olivine (see section 4.1). For more information on the bulk-rock analytical procedure using XRF and ICP-MS analysis we refer to Molendijk *et al.* (2024). All discussed samples correspond to the most primitive (olivine-dominated) lithologies reported for Nyiragongo and should therefore contain the most primary signatures of this system. We crushed the whole-rock samples and extracted their olivine crystals, after which these were mounted in 1-inch epoxy mounts named mount 1, 2, 3, 4, and 161. An overview of the contents of each mount is given in Supplementary Material 2.

3.2. Electron microprobe analyses

Electron microprobe analyses (EMPA) was performed at KU Leuven on mounts 1, 2, 3, and 4 using a JEOL JXA-8540F microprobe. These runs targeted olivine and chromite inclusions. Operating conditions were 20 kV for all analyses using a nominal beam current of 15 – 20 nA and a standard beam size of 10 µm. Analyses of olivine-chromite couples were performed at >20 µm from phase margins where possible in order to avoid potential effects of secondary fluorescence. On-peak counting times were 20 seconds for all elements and 10 seconds of background on both sides of the peak. Primary standardization was performed using albite (Al), diopide (Si, Ca), hematite (Fe), rutile (Ti), chromium-oxide (Cr), rhondonite (Mn), and MongOl Sh11-2 olivine (Mg, Ni) (Batanov*a et al*., 2019). San Carlos olivine and Smithsonian chromite were repeatedly measured as secondary standards to evaluate accuracy.

A subset of olivine crystals from mount 3 as well as the entirety of mount 161 were measured at Utrecht University using an identical system. These measurements used a nominal beam current of 200 nA but applied otherwise similar settings. An overview of all analyses is provided in Supplementary Material 1. Relative errors on major element concentrations based on secondary standard analyses are generally at < 5% for all concentrations above 0.5 wt.%. For 15 nA analyses, median errors are 0.6% for SiO_2, 11.2% for Al_2O_3, 0.4% for MgO, 1.9% for FeO, 6.5% for CaO, 8.9% for MnO, 5.0% for NiO, and 54.9% for Cr_2O_3 at these concentrations. For 200 nA analyses, these errors are instead 0.2% for SiO_2, 9.3% for Al_2O_3, 0.2% for MgO, 0.4% for FeO, 6.0% for CaO, 5.1% for MnO, 1.3% for NiO, and 28.4% for Cr_2O_3. As such, LA-ICP-MS values (see section 3.3) are preferred for Cr and most Al analyses. A systematic underestimation of CaO was observed for analyses performed at KU Leuven. These have been filtered out accordingly, giving preference to LA-ICP-MS values.

3.3. LA-ICP-MS

Olivine crystals in mounts 1, 2, 3, and 161 were analysed by LA-ICP-MS at KU Leuven. Mount 4 was excluded due to a low average crystal size impairing measurement. Olivine crystals were measured as 30 seconds of line analysis with a fluence of 7.0 J/cm^2, a repetition rate of 8 Hz, and a spot size of 110 µm following a pre-rastering with a fluence of 4.0 J/cm^2. Pre- and post-measurement backgrounds were set to 30 to 45 seconds.

The NIST-612 reference standard was used for drift correction whereas external standardization and signal stability evaluations were performed using the MongOl Sh11-2 international reference standard (Batanov*a et al*., 2019), indicating relative errors of < 15% for minor element and transition metals, with the exceptions of Cu (124%) and Zn (22%). Cu will therefore not be considered further. Relative errors of particularly incompatible elements (< 0.1 μg/g; Sr, Y, Zr, HREE) are generally < 20%, with an average of 15%. No reference values are available for LREE and middle rare earth elements (MREE) in olivine.

All data was filtered for sub-detection limit measurements as well as potential influence of mineral and melt inclusions. For internal standardization we used EMPA derived values for ^{29}Si (olivine).

4. RESULTS

4.1. Petrography and whole-rock chemistry

As discussed by Molendijk *et al.* (2024), the olivine-dominated lithologies of Nyiragongo can be petrographically and geochemically subdivided into five categories. These will be shortly described here in order of increasing MgO-content, and are displayed visually in Fig. 3.

- Micro-olivine basalts (8.4 - 8.8 wt.% MgO; moB-types) are the least primitive sample type and include mostly microphenocrysts (≤ 500 μm in diameter; Fig. 3a) of olivine and clinopyroxene in a cryptocrystalline matrix of clinopyroxene, nepheline, and leucite. The olivine crystals in these samples are frequently reverse-zoned in contrast with those from other groups.
- Olivine-cpx basalts (9.0 – 10.7 wt.% MgO; OCB-types) include normally zoned olivine and clinopyroxene phenocrysts (> 1 mm in size) in a matrix similar to that of the moB-types.
- Olivine-melilite basalts (9.5 – 13.4 wt.% MgO; OMB-types; Fig. 3b) are petrographically similar to the OCB-types, but include more significant amounts of melilite in both the matrix and phenocryst populations, replacing clinopyroxene. Olivine crystals in OMB-type (and OCB-type) samples are frequently normally zoned.
- Picritic melilite basalts (18.8 – 23.5 wt.% MgO; PMB-types) essentially represent OMB-types with excess olivine, in this case lacking zoning features. They are poor in clinopyroxene and have a matrix composed of melilite, nepheline, and clinopyroxene, in

that order of abundance (Fig. 3c). Chromite is common in olivine crystals from this group. Further petrographic analysis of these samples showed the presence of anhedral, green aegirine crystals (Supplementary Material 2).

- The most Mg-rich (26.4 – 29.8 wt.% MgO; P-type) subgroup reported by Molendijk *et al.* (2024) is simply called 'picrites'. This group of samples has a phenocryst population that almost exclusively contains olivine, with minor chromite and rare clinopyroxene (Fig. 3d). The matrix of these samples is still clinopyroxene-rich, with subordinate olivine and nepheline but lacks melilite. Olivine from these samples is also homogeneous and may contain chromite.

The complete whole-rock compositions obtained by XRF and ICP-MS of all samples discussed here can be found in Table 1 and were previously presented by Molendijk *et al.* (2024). They show a universally silica-undersaturated (SiO_2 = 37 – 41 wt.%) and alkaline ($Na_2O + K_2O$ = 1.7 – 6.1 wt.%) chemistry (Fig. 2a). These lithologies are additionally rich in Al_2O_3 (7 – 13 wt.%), $Fe_2O_{3(T)}$ (12 – 14 wt.%), and CaO (8 – 16 wt.%), which all increase with decreasing MgO (8 – 28 wt.%) content and Mg# ($100*Mg/[Mg+Fe^{2+}]$). Additionally, we can identify two groups from their P_2O_5 contents (0.5 – 0.8 and 1.3 – 1.5 wt.%). In terms of trace elements, the primitive Nyiragongo lavas are large ion lithophile elements (LILE) and LREE enriched (40 – 200 times primitive mantle values), with a high LREE/HREE ratio ($[La/Lu]_N$ = 23 – 54, where $_N$ represents normalization to primitive mantle values of Sun and McDonough (1989)) (Fig. 2b; Table 1; Hertogen *et al.*, 1985; Platz *et al.*, 2004; Chakrabarti *et al.*, 2009a; Molendijk *et al.*, 2024). Additional noteworthy trace element signatures include high Th ($[Th]_N$ = 47 – 131) and U ($[U]_N$ = 56 – 202) concentrations with an exceptionally high Th/U ratio (2.3 – 3.4), as well as negative anomalies for Pb, Zr, Hf, Ti, and Y (Table 1; Molendijk *et al.*, 2024).

Table 1 Major and trace element compositions of whole-rock samples from Molendijk et al. (2024) referred to in this study. Samples for which olivine data has been previously reported by Molendijk et al. (2024) are indicated with '' following the sample name. Abbreviations for sample subgroups are explained in the petrography and whole-rock chemistry section 4.1. $Fe_2O_{3(T)}$ represents all iron interpreted as trivalent. Cone locations can be found in Fig. 1c. Trace elements are derived from ICP-MS analysis apart from Zr and Nb, for which XRF values are used. Trace elements of sample Ny20-008 are entirely derived from XRF analysis.*

Sample	**Ny17-132***	**Ny17-140***	**Ny17-141**	**Ny17-142**	**Ny17-160***	**Ny17-161**	**Ny17-163**	**Ny17-164***	**Ny17-171***	**Ny17-178***	**Ny17-179***	**Ny17-209***	**Ny17-217***	**Ny17-218***	**Ny20-008***
Sample subgroup	P-type	P-type	P-type	P-type	OMB-type	OMB-type	PMB-type	PMB-type	PMB-type	OMB-type	OMB-type	OCB-type	moB-type	moB-type	PMB-type
Associated cone	Muja	Muja	Muja	Muja	Rushayo	Rushayo	Kaboro	Kaboro	Nyabusa	Lac Vert	Lac Vert	Mudjoga	Mugara	Mugara	Nyabusa
wt.%															
SiO_2	41.0	41.1	41.1	41.1	38.6	39.2	37.4	38.3	37.6	39.7	39.4	39.6	41.3	41.3	38.6
TiO_2	1.3	1.3	1.3	1.3	3.2	3.1	1.9	2.1	1.9	3.2	3.2	3.5	3.4	3.5	1.8
Al_2O_3	6.7	6.7	7.0	6.9	10.6	10.5	8.2	8.8	7.8	10.9	10.8	11.5	12.5	12.6	7.6
$Fe_2O_{3(T)}$	12.3	12.0	12.2	12.2	12.8	12.6	11.2	11.7	11.6	12.6	12.7	13.8	13.3	13.2	11.6
MnO	0.2	0.2	0.2	0.2	0.2	0.2	0.2	0.2	0.2	0.2	0.2	0.2	0.2	0.2	0.2
MgO	28.1	28.0	27.5	27.6	10.8	10.9	19.6	18.7	20.7	11.3	11.5	10.0	8.5	8.4	23.0
CaO	8.2	8.0	8.2	8.2	16.2	16.1	14.7	13.6	14.6	15.7	15.8	15.3	15.0	15.1	12.8
Na_2O	1.0	1.3	1.2	1.2	3.0	3.0	3.2	2.9	2.2	3.6	2.4	2.6	2.4	2.3	1.5
K_2O	0.7	0.9	1.0	0.9	3.1	2.9	2.1	2.2	2.0	1.5	2.6	2.5	2.6	2.6	1.7
P_2O_5	0.5	0.5	0.5	0.5	1.5	1.5	1.4	1.5	1.4	1.4	1.3	1.0	0.8	0.8	1.2
Mg#	81.9	82.2	81.7	81.8	62.5	63.0	77.6	76.0	78.0	63.9	64.2	58.9	55.7	55.7	79.7
ppm															
Sc	23	22	24	22	24	24	25	27	26	25	24	28	33	33	-
V	160	160	160	160	390	380	250	270	270	360	370	410	360	360	210
Cr	2720	2780	2750	2570	290	260	830	700	770	320	290	280	190	170	1350
Co	99	93	93	92	56	53	68	67	75	50	53	52	47	45	-
Ni	970	910	900	880	190	170	640	570	660	160	180	150	98	91	-
Cu	31	62	49	65	100	100	69	68	92	96	103	69	68	70	-
Zn	69	70	72	71	83	80	65	69	63	81	88	85	84	83	-
Rb	27	26	26	26	81	80	48	59	49	42	59	74	70	65	30
Sr	590	590	600	610	2200	2150	2080	1920	1790	1740	2010	1350	1230	1250	1130
Y	16	16	16	17	28	27	27	29	23	25	25	27	25	25	23
Zr	140	140	140	140	270	270	200	210	200	260	260	280	260	260	180
Nb	37	38	38	38	110	120	98	105	77	110	110	96	83	82	50
Cs	0.3	0.4	0.3	0.3	0.7	0.7	0.5	0.5	0.5	0.9	0.5	0.7	0.7	0.7	-
Ba	350	340	340	340	1230	1210	950	1010	860	1240	1230	1330	1330	1360	-
La	40	40	39	38	120	120	130	140	100	120	120	100	87	89	-
Ce	88	87	85	83	240	240	250	270	210	240	240	210	180	180	-
Pr	10	10	10	9.5	27	26	26	28	22	26	26	23	20	20	-
Nd	36	36	36	35	100	100	96	110	86	97	99	88	78	79	-
Sm	6.2	6.2	6.0	5.9	16	16	14	16	13	15	15	14	13	13	-

Eu	1.7	1.7	1.7	1.7	4.4	4.3	3.9	4.3	3.7	4.1	4.2	3.9	3.5	3.6	-
Gd	4.8	4.7	4.8	4.7	12	12	11	12	10	11	11	11	10	10	-
Tb	-	-	-	-	1.3	1.3	1.2	1.3	1.1	1.3	1.3	1.3	1.2	1.2	-
Dy	3.2	3.2	3.2	3.2	6.3	6.2	5.8	6.3	5.2	6.2	6.3	6.4	6.2	6.3	-
Ho	0.6	0.6	0.6	0.6	1.0	1.0	1.0	1.0	0.9	1.0	1.1	1.1	1.1	1.1	-
Er	1.4	1.4	1.4	1.4	2.7	2.7	2.5	2.7	2.2	2.7	2.7	2.8	2.8	2.9	-
Tm	-	-	-	-	0.3	0.3	0.3	0.3	0.3	0.3	0.3	0.3	0.4	0.4	-
Yb	1.2	1.2	1.1	1.2	1.9	1.9	1.8	2.0	1.6	2.0	2.0	2.1	2.2	2.2	-
Lu	0.2	0.2	0.2	0.2	0.3	0.3	0.3	0.3	0.2	0.3	0.3	0.3	0.3	0.3	-
Hf	3.0	2.9	3.1	3.1	5.6	5.5	4.3	2.1	4.4	6.1	6.0	7.4	7.0	7.3	-
Pb	6.9	1.9	2.9	3.0	2.7	2.5	4.6	2.5	2.4	3.3	3.4	2.6	3.4	3.5	-
Th	4.0	4.1	4.2	4.1	9.6	9.5	10	11	7.0	11	11	8.7	8.1	8.1	-
U	1.2	1.3	1.2	1.2	4.0	4.0	3.9	4.1	2.7	3.7	4.3	3.7	2.4	2.4	-

264

265

Table 2 Mean compositions of primitive olivine crystals for each host sample-type including 1σ standard deviation. Major elements are derived from electron microprobe analysis whereas trace elements are derived from LA-ICP-MS analysis unless indicated otherwise by the notation (EMPA). A more detailed overview of all analyses can be found in Supplementary Material 1.

Sample-Type	**moB-type**	**1σ**	**OCB-type**	**1σ**	**OMB-type**	**1σ**	**PMB-type**	**1σ**	**P-type**	**1σ**
SiO_2	40.1	0.3	40.1	0.2	40.4	0.3	40.6	0.5	40.5	0.3
MgO	45.5	1.3	46.7	0.8	47.6	0.7	48.8	1.3	48.7	0.5
FeO	14.0	1.7	12.0	1.0	11.4	0.8	10.1	1.4	10.4	0.6
Fo	85.3	1.8	87.4	1.1	88.1	0.8	89.6	1.5	89.4	0.6
Ppm↓										
Ca (EMPA)	3743	336	3663	680	3213	272	2256	1011	2764	340
Ca (LA)	3222	495	3431	661	3021	417	2338	704	2531	395
Ni (EMPA)	803	770	1550	417	1543	471	1973	837	1628	880
Ni (LA)	1241	233	1629	215	1719	195	1926	358	1995	279
Mn (EMPA)	1940	251	1669	226	1527	174	1414	292	1330	177
Mn (LA)	2056	275	1824	253	1624	175	1593	359	1496	180
Cr (EMPA)	85	107	182	92	236	116	320	239	360	245
Cr (LA)	162	102	210	86	308	72	299	133	430	96
Al (EMPA)	216	136	204	66	202	57	225	132	208	95
Al (LA)	227	24	229	64	225	44	244	89	289	63
Sc	5.3	1.2	5.5	0.9	5.8	0.8	4.8	1.3	5.0	0.6
Ti	171	39	112	36	124	23	98	19	96	24
V	4.9	0.6	3.9	0.8	4.7	0.6	4.1	1.2	4.6	0.7
Co	175	17	153	15	158	13	150	20	163	17
Zn	98	14	78	9	71	8	74	12	74	10
Ppb↓										
Rb	5	3	4	3	12	35	4	4	5	4
Sr	82	58	38	19	36	23	41	18	45	27
Y	150	28	118	27	83	14	105	28	108	20
Zr	77	39	61	18	55	15	71	33	54	15
Nb	7	5	7	7	2	2	8	11	5	6
Cs	2	0.2	1	0.3	2	0.6	1	0.8	1	0.6
Ba	54	47	45	41	28	29	23	16	29	30
La	4	3	1	0.8	1	1	2	2	1	1
Ce	4	3	3	2	3	2	6	4	3	3
Pr	2	1	1	1	0.5	0.5	0.9	0.8	1	0.8
Nd	7	6	5	3	3	1	6	5	4	3
Sm	4	2	3	2	2	0.9	3	1	2	1
Eu	2	0.6	1	0.5	1	0.6	1	0.6	1	0.6
Gd	6	4	7	2	5	2	6	2	6	2
Dy	15	4	14	3	10	2	12	3	13	3
Ho	5	2	4	1	3	1	4	1	4	1
Er	19	5	17	5	12	2	16	5	15	4
Tm	4	1	3	0.9	2	0.6	3	1	3	1
Yb	36	6	31	7	21	5	28	8	27	6
Lu	8	2	6	1	4	1	6	2	5	1
Hf	3	2	2	1	2	1	3	1	3	2
Ta	0.6	0.4	0.5	0.4	0.3	0.4	0.4	0.5	0.4	0.4
Th	1.0	0.7	0.5	0.4	0.4	0.5	0.4	0.5	0.9	0.8
U	3	2	0.2	0.2	0.5	1	0.5	1	0.8	1

4.2. Olivine geochemistry

The exact compositions of individual olivine crystals can be found in Supplementary Material 1. Mean compositions are presented in Table 2, and a short summary thereof is provided below.

Measured olivine grains have forsterite (Fo = 100*Mg/(Mg+Fe)) contents ranging from 82.4 to 91.7 (Fig. 4a), covering the majority of the core compositions reported by Molendijk *et al.* (2024). Fo content correlates positively with Ni (830 to 3230 ppm; Fig. 5a), Cr (5 to 839 ppm), and Al (21 to 464 ppm but mainly > 100 ppm). Negative correlations with Fo are observed for Ca (1892 to 4576 ppm but with low-concentration outliers down to 111 ppm; Fig. 5b) and Mn (856 – 2262 ppm; Fig. 5c). In line with whole-rock compositions, the average composition of olivine from the P- and PMB-type samples is (slightly) more primitive than those of the non-picritic varieties. However, whereas the P-type samples are significantly more Mg-rich than the PMB-types, the compositions of their olivine cargoes overlap greatly, with the latter type including the most Fo-rich compositions. This likely reflects that the P-type samples contain a higher olivine/matrix ratio than the PMB-types, and that the P-type matrix composition is slightly less M-rich than that of the PMB-types.

Other transition metals do not follow the patterns of Ni and Cr, with Co (113 – 211 ppm), Zn (53 – 117 ppm), Sc (2.2 – 7.9 ppm), and V (0.7 – 6.6 ppm) either staying relatively constant or decreasing slightly with Fo content. Vanadium in this case is very low in olivine from picritic melilite basalt samples, correlating with low Al and Ti values. In the ppb range we find Y to be negatively correlated with Fo at concentrations of up to 202 ppb, but the similarly enriched Zr shows no correlation. LILE are variably enriched in the olivine crystals but without a reference material and only few analyses, it is impossible to gauge the accuracy of these measurements. REE concentrations increase from LREE to HREE, with median primitive-mantle normalized (Sun and McDonough, 1989) La concentrations stretching from 1×10^{-3} to 4×10^{-3} (Table 2) and average normalized Lu concentrations between 5.6×10^{-2} and 9.3×10^{-2}.

4.3. Thermometry

Chromite was analysed in a total of seven samples of the PMB- and P-type groups. Trivalent iron contents were calculated using charge balance on a four-oxygen basis using the method of Droop

(1987). Crystals had Cr# (100*Cr/[Cr + Al]) values stretching from 30 to 86, with a median of 54 regardless of olivine host (Fig. 4b). Similarly, their Mg# range from 50 to 74, with a median of 67. We applied the thermometers of Zhang *et al*. (2023), which are three-fold: equations 5, 7, and 8 can all be used to estimate temperatures using different parameters. Equation 5 uses the spinel composition and Al-equilibrium between olivine and spinel, equation 7 uses the Al-equilibrium in addition to the chromite Cr#, and equation 8 uses the olivine-spinel Cr equilibrium in addition to the parameters of equation 7. As a consequence of their different inputs, these equations are sensitive to different parameters and therefore it is important to choose the best equation for each olivine-chromite couple. This is done with a z-test, which finds the equation with the lowest root-mean-square-error for a specific crystal pair. Application of this test and the appropriate thermometric equations results in a temperature range of 1079 to 1347 °C (Fig. 6), corresponding to the results of equations 5 (84%), 7 (1%), and 8 (14%). The crystallization temperatures clearly correlate with the host olivine's forsterite content and agree approximately with the temperatures estimated for Siqueiros MORB lavas (1182 – 1295 °C) and those of Iceland (1175 – 1327 °C) (Fig. 6; Zhang *et al.*, 2023). Comparison with systems which are more purely plume-related like the large igneous province of Etendeka (1219 to 1417 °C) and the highly primary Tortugal suite of the Caribbean large igneous province (1276 – 1502 °C) (Zhang *et al.*, 2023) shows that these sites generally report higher temperatures of crystallization than Nyiragongo. Olivine from Nyiragongo therefore reflects a thermal state of its mantle source that in line with either ambient (MORB) mantle or one that is mildly thermally elevated (Iceland).

Composition	Mg_74	Mg_70
%Olivine removed	*22*	*15*
wt.%		
SiO_2	38.0	38.2
TiO_2	2.6	2.4
Al_2O_3	11.1	10.3
FeO	8.7	8.7
Fe_2O_3	2.4	2.2
MnO	0.2	0.2
MgO	11.4	13.9
CaO	17.0	15.9
Na_2O	3.6	3.3
K_2O	2.8	2.6
P_2O_5	1.9	1.7
Mg#	70.1	74.0
ppm		
Sc	33	31
V	335	312
Cr	796	764
Co	47	54
Ni	228	347
Cu	85	79
Zn	68	69
Rb	74	69
Sr	2399	2236
Y	36	33
Zr	266	248
Nb	131	122
Cs	0.6	0.6
Ba	1258	1172
La	176	164
Ce	333	310
Pr	35	33
Nd	132	123
Sm	19	18
Eu	5.4	5.0
Gd	15	14
Tb	1.7	1.6
Dy	7.9	7.3
Ho	1.3	1.2
Er	3.4	3.2
Tm	0.4	0.4
Yb	2.5	2.3
Lu	0.3	0.3
Hf	5.3	4.9
Pb	3.1	2.9
Th	14	13
U	5.1	4.8

Table 3 Compositions of hypothetical parental melts for Nyiragongo based on removal of PMB-type olivine (Table 2) from PMB-type sample Ny17-164. Trace elements for which olivine data was unavailable were not included.

319

320

5. DISCUSSION

5.1. Parental melt reconstruction

In order to establish a mantle source, we first need to identify the most primitive melt in the system, preferably that from which the most primitive olivine has crystallized. We approach this by first establishing the Mg# of this melt by taking the most Fo-rich crystal in our collection (Fo = 91.7) and calculating the equilibrium melt Mg# using the Mg-Fe exchange coefficient $K_{D\,Fe-Mg}^{ol-liq}$. We can conclude that this olivine crystal (and by extension, others of similar Fo-content) is an antecryst or autocryst based on its high Ca content (1893 ppm; Fig 5b), which is incompatible with mantle-derived olivine reported from the EARS (e.g., Koornneef *et al.*, 2009). For the exact value of $K_{D\,Fe-Mg}^{ol-liq}$ required for equilibrium calculations we consulted the experimental work of Molendijk *et al.* (2023) who performed experiments using compositions of Nyiragongo which produced olivine in equilibrium with melt. These experiments were performed under oxygen fugacity conditions buffered to the quartz-fayalite-magnetite (QFM) equilibrium (the best currently available approximation for Nyiragongo, based on observations from the nearby system of Nyamulagira (Head *et al.*, 2018)), and produced $K_{D\,Fe-Mg}^{ol-liq}$ values between 0.21 and 0.26 (Molendijk *et al.*, 2023). Such low K_D values are not unusual for highly alkali-rich magmatic systems, due to the effects of Na and K (e.g., Gee and Sack, 1988; Toplis, 2005). Applying this K_D value to the 91.7 forsterite olivine results in an equilibrium melt Mg# of 70 to 74, between OMB- and PMB-type whole-rock compositions (still assuming QFM-buffered oxygen fugacity conditions, calculating the whole-rock Fe^{2+}/Fe^{3+} ratios with the method of Kress and Carmichael (1991) at 1300 °C). In order to establish an approximation for all other elemental concentrations in the parental melt we can assume that the majority of crystallization between OMB- and PMB-type melts was olivine, following the work of Molendijk *et al.* (2024). Under this assumption we can mathematically subtract olivine (PMB composition from Table 2; Fo = 89.6) from a PMB-type whole-rock until the hypothetical melt reaches an Mg# of 70 and 74. For this approach we picked PMB-type magma Ny17-164, as this is the lowest Mg# PMB-type available in the work of Molendijk *et al.* (2024). As before, we performed this approach assuming a temperature of 1300 °C, based on olivine crystallization temperatures (Fig. 6), and with redox conditions buffered to

QFM to calculate Fe^{2+}/Fe^{3+} ratios with the method of Kress and Carmichael (1991). The resulting hypothetical melts are listed in Table 3 and will be referred to as Mg_70 and Mg_74, matching their Mg#.

5.2. Identifying mantle source components – Chemical proxies

In this section we will attempt to ascertain the mantle lithology supplying Nyiragongo's plumbing system using chemical proxies. Constituents of any given mineral assemblage that melts in the mantle will be retained in the melts they produce, which allows us to back-track from erupted melt composition to melting assemblage. In contrast, the partitioning of trace elements between melt and restite can cause enrichment or depletion signatures in ascending melts, which may be imprinted on early crystallizing olivine (Sobolev *et al.*, 2005, 2007, Foley *et al.*, 2011, 2013; Barker *et al.*, 2014; Ammannati *et al.*, 2016; Howarth and Harris, 2017; Veter *et al.*, 2017; Neave *et al.*, 2018; Wong *et al.*, 2022; Vozniak *et al.*, 2023). While recent work (Matzen *et al.*, 2013, 2017b; Gleeson and Gibson, 2019) has indicated that the approach of simply using olivine trace element compositions and element partitioning trends to infer mantle assemblages uses an oversimplified view of trace element distribution systematics, the basic principle can still be applied under critical evaluation. In the following section we will discuss individual mineral contributions to erupted magmas from the mantle source, and the evidence pointing at their presence or absence. The mineral species discussed were chosen based on previous studies regarding silica-undersaturated volcanic systems and to answer specific research questions:

1) Peridotite and pyroxenite are the two main lithologies found in the upper mantle and variations in their proportions likely make up the bulk of mantle heterogeneity (e.g., Sobolev *et al.*, 2005; Matzen *et al.*, 2017b). Mantle pyroxenite would suggest recycling of subducted slabs under the craton.
2) Mantle phlogopite has been found at nearby Toro-Ankole (e.g., Bell and Powell, 1969; Pitcavage *et al.*, 2021; Innocenzi *et al.*, 2024) and is frequently used to explain high-K lavas. This is a hydrated phase suggesting an origin through metasomatism.
3) Amphibole is a similarly hydrated phase commonly associated with phlogopite, and is suggested to provide a more Na-, and Ca-rich signature in similarly silica-undersaturated,

alkali-rich systems (Sorbadere *et al.*, 2013b; Bracco *et al.*, 2023). It is stable up to 2.5 GPa (Class and Goldstein, 1997; Niida and Green, 1999; Conceiçao and Green, 2004), providing a depth constraint.

4) Silica-undersaturation and high calcium concentrations are commonly known from carbonatites (Peterson, 1990; Klaudius and Keller, 2006), thought to be generated in part through carbonate metasomatism (Peterson, 1990). This feature has been reported at the EARS and would explain the high CO_2 emissions from the rift (Foley and Fischer, 2017; Aiuppa *et al.*, 2021).
5) High P_2O_5 concentrations as well as significant variability in concentrations of this oxide between similarly primitive samples suggests that a P_2O_5 source such as apatite may be present in the mantle source of Nyiragongo. Evidence for this already exists for the broader EARS (Lloyd *et al.*, 1985; Koornneef *et al.*, 2009)
6) Lastly, in order to establish a depth of melting, the dominant aluminosilicate phase must be established, most likely being spinel (< ~120 km) or garnet (> ~120 km) (Ziberna *et al.*, 2013).

5.2.1. Peridotite versus pyroxenite components

Pyroxenites are thought to be the second most common mantle lithology, produced through recycling of subducted eclogitic crust and reaction with ambient olivine-rich mantle (Yaxley and Green, 1998; Sobolev *et al.*, 2005; Herzberg, 2006). In the primitive melts of Nyiragongo the melting of clinopyroxene can be inferred through high whole-rock CaO concentrations, which are thought to increase during clinopyroxene melting until the phase is consumed (Lambart *et al.*, 2009, 2013). Low SiO_2 concentrations, FeO enrichments, and high CaO/Al_2O_3 ratios can also be derived from high degrees of clinopyroxene melting, and are observed in the Nyiragongo lavas (Table 1). Pyroxenite domains can be identified using olivine trace element contents because low Ni retention by restite pyroxene during melting results in a higher concentration of Ni in extracted magmas, which is passed on to crystallizing olivine (Sobolev *et al.*, 2005, 2007). The most prominent identifiers of a pyroxenite restite are elevated (> 20) Ni/Co and depleted (< 13) Mn/Zn ratios (Howarth and Harris, 2017), neither of which are observed for the Nyiragongo olivine (Fig. 7d) (Sobolev *et al.*, 2007), suggesting an olivine-dominated restite.

Nevertheless, concerns have been raised with regards to the validity of this argument, due to the effects of temperature-, pressure-, and composition on partitioning coefficients in olivine, especially that of Ni (Mysen, 1979; Foley *et al.*, 2013; Matzen *et al.*, 2013, 2017b, 2017a; Gleeson and Gibson, 2019). Indeed, Ni partitioning into olivine is increased at low pressures and high alkalinity, potentially causing overestimation of pyroxenite influences in deep melting regimes or highly alkaline systems (Foley *et al.*, 2013; Matzen *et al.*, 2017b). Deep melting concurrently (and indirectly) causes higher Mn retention, either through changes in olivine partitioning or retention in garnet, further amplifying this. Lastly, the work of Gleeson and Gibson (2019) shows that apparent pyroxenite signatures in olivine can also be generated through recharge and mixing, which may buffer Ni concentrations. Luckily these pitfalls, though likely applicable to Nyiragongo, would all amplify a pyroxenite signal, which is opposite to what we currently observe. Indeed, these additional influences on olivine partitioning only serve to reaffirm the pyroxene-poor restite signal we observe.

As such, the whole-rock signals observed at Nyiragongo point to potential clinopyroxene melting, but the majority of the restite with which the melt equilibrates proves to be olivine-rich.

5.2.2. Phlogopite components

Phlogopite is the source mineral which has been most commonly inferred for Nyiragongo magmas (Chakrabarti *et al.*, 2009a, 2009b; Condomines *et al.*, 2015; Minissale *et al.*, 2022), and magmatism in the western EARS more generally. It is frequently used to explain ultra-potassic volcanism due to supplying abundant potassium as it melts (Nikogosian and van Bergen, 2010; Condamine and Médard, 2014; Bracco *et al.*, 2023). In practice this phase most commonly presents itself in metasomatic veins (Foley, 1992), which are commonly emplaced either through subduction-related sediment recycling (Ammannati *et al.*, 2016; Bracco *et al.*, 2023) or crystallization from ascending small-degree melts (Pilet *et al.*, 2008). As mentioned earlier, phlogopite melting in the VVP is most commonly inferred from low K/Rb ratios and high LILE concentrations in the Nyiragongo lavas since these elements concentrate in phlogopite (LaTourrette *et al.*, 1995; Baudouin and Parat, 2020; Condamine *et al.*, 2022). Rb and Ba in particular are present at sufficient concentrations in phlogopite that they are likely to be enriched in the melt even if some phlogopite remains in the restite. especially at high degrees of melting. Phlogopite is more difficult to trace using olivine trace elements, though Foley *et al.* (2013) have indicated that high Zn and Li (not measured here) may be useful proxies in the case of crustal-

recycling derived phlogopite, due to the high concentrations of these elements in subducted sediments. Comparatively low olivine Zn concentrations compared to Mediterranean samples may thus indicate that any phlogopite under the VVP is not derived from slab sediments (Fig. 7f).

Phlogopite expresses high D_{Ni} (30 - 84) values at low pressure (1 GPa), but these decrease at higher pressures such as are commonly attributed to phlogopite stability in the region (Class and Goldstein, 1997; Green and Falloon, 1998; Chakrabarti *et al.*, 2009a; Foley *et al.*, 2012), down to values similar to those of olivine (5.4 – 7.8), making it difficult to deconvolute a phlogopite signature from that of olivine (Condamine *et al.*, 2022). Indeed, the high D_{Ni}/D_{Co} (4 – 10) ratio in phlogopite may be attributed to the previously discussed peridotite signature.

All things considered, the K and LILE enrichment signatures in Nyiragongo lavas suggest a significant proportion of phlogopite in the melting assemblage, but its presence in the restite is more difficult to ascertain using mineral compositions as of now.

5.2.3. Amphibole components

Pargasitic amphibole is another hydrous mineral associated with metasomatic veins, often found together with phlogopite (Lloyd, 1981; Foley, 2008; Pilet *et al.*, 2008), and typically stable up to a pressure of ~2.5 GPa and temperature of ~1100 °C (Class and Goldstein, 1997; Niida and Green, 1999; Conceiçao and Green, 2004). Experimental studies have shown that low degree partial melts from amphibole-bearing peridotites can produce nepheline-normative melts that are exceedingly Ca- and Na-rich with relatively low SiO_2 concentrations (Médard *et al.*, 2006; Sorbadere *et al.*, 2013a), providing an explanation for the high-Ca signature in Nyiragongo olivine.

Xenoliths found in the western branch of Tanzanian Craton sometimes present low abundances of amphibole, though it is much rarer than phlogopite (Lloyd, 1985; Dawson and Smith, 1988; Muravyeva and Senin, 2016, 2018). A high phlogopite/amphibole ratio may indicate that the mantle source is located at great depth (>2.5 GPa), outside of the amphibole stability window, coinciding with estimates of melt segregation in the VVP (Pitcavage *et al.*, 2021)

The geochemical signature of lithospheric amphibole is similar to that of clinopyroxene, being a Ca-, and Al-rich phase with high partition coefficients for MREE and HREE, transition metals (Sc, Ti, Mn, Co, Ni, Y) and a particular preference for Ca, Co, and Sc (Condamine *et al.*, 2022). Like phlogopite, amphibole is rapidly consumed in the melting of metasomatic mantle domains (Médard *et al.*, 2006; Sorbadere *et al.*, 2013a; Condamine and Médard, 2014; Condamine *et al.*, 2016), meaning it is often completely exhausted during melting and absent from the restite.

Amphibole has been suggested as a source component for the VVP as well as Toro Ankole (Pitcavage *et al.*, 2021) based on low Rb/Sr (0.02 – 0.06) and elevated Ba/Rb (12.8 – 29.8), Sm/Hf (1.8 – 7.6), and Zr/Nb (2.0 – 3.7) ratios (Fig. 7b). However, while these ratios can all indicate substantial melting of amphibole, they may also be readily explained by clinopyroxene melting or the presence of phlogopite in the restite (Marks *et al.*, 2004; Condamine *et al.*, 2022). High degrees of amphibole melting would generate high K/Rb ratios, high concentrations of MREE and HREE, and low Dy/Dy* ratios at low Dy/Yb values (Davidson *et al.*, 2013), which are not conclusively observed in Nyiragongo volcanics (Table 1; Coltorti *et al.*, 2007; Condamine *et al.*, 2022; Supplementary Material 3). As a result, amphibole contributions cannot be excluded, but are likely minor if present.

5.2.4. Carbonated components

Previous geochemical arguments for direct carbonate involvement at Nyiragongo centre around high Zr/Hf ratios (Dupuy *et al.*, 1992; Chakrabarti *et al.*, 2009a; Molendijk *et al.*, 2024). However, it was pointed out by Condomines *et al.* (2015) that such ratios may also be generated by different metasomatic agents, referring to the work of Veksler *et al.* (2012).

Instead, the high-Ca signature observed in Nyiragongo olivine, comparable to carbonatites (Vozniak *et al.*, 2023) and ultrapotassic rocks (Ammannati *et al.*, 2016; Bracco *et al.*, 2023), provides more robust evidence for calcium-rich phases of the mantle source. Our crystal compositions most closely resemble those of the ultrapotassic rocks from Vulsini in Italy (Bracco *et al.*, 2023), which are CaO enriched due to the melting of calcium-bearing amphibole, clinopyroxene, and apatite rather than pure carbonate domains.

The high whole-rock P_2O_5 content in primitive samples (Table 1) suggests apatite to be a likely calcium source for the Nyiragongo magmas. Melting mantle apatite would supply (1) a high-Ca signature reported for our olivine, (2) the high P_2O_5 concentrations in primitive melts, and (3) the Th/U and LREE enrichment characteristic of all Nyiragongo volcanics (Hertogen *et al.*, 1985; Platz *et al.*, 2004; Minissale *et al.*, 2019; Molendijk *et al.*, 2024).

Significant variability in P_2O_5 exists among the primitive lithologies of Nyiragongo, which Molendijk *et al.* (2024) argued to reflect mantle heterogeneity, and may well reflect variable abundances of apatite. The correlation between LREE and P_2O_5 concentrations (Table 1; Fig. 7c) corroborates this idea. Mantle apatite is not uncommon, having been reported in phlogopite-

holding xenoliths from around the Tanzanian craton (Lloyd *et al.*, 1985), as well as other (alkaline) volcanic provinces (e.g., O'Reilly and Griffin, 2000).

5.2.5. Cr-spinel / Garnet components

Among the possible Al-bearing mantle phases (plagioclase, Cr-spinel, garnet) both garnet and Cr-spinel have been observed in mantle xenoliths from around the EARS (Lloyd *et al.*, 1985; Koornneef *et al.*, 2009; Gibson *et al.*, 2013; Baptiste *et al.*, 2015; Muravyeva and Senin, 2016). These phases are commonly minor constituents with major roles in trace element distribution, and the transition from spinel to garnet stability signifies a transition to higher pressures (> ~2.5 GPa) (Robinson and Wood, 1998; Klemme and O'Neill, 2000). Cr-spinel contributions in the restite are generally recognised through a high Cr and Ni retention due to the high partition coefficient of these elements in chromite (Foley *et al.*, 2013), whereas garnet has a high partition coefficient for HREE, which it preferentially retains (e.g, Hauri *et al.*, 1994; Salters and Longhi, 1999). The olivine data represented here shows no depletion on Ni nor Cr (Fig. 7) but lavas from Nyiragongo are consistently poor in HREE compared to MREE (Table 1; $(Dy/Yb)_N$ = 1.8 – 2.2). Overall, this indicates that garnet is the more likely Al-bearing phase in the source region of Nyiragongo.

5.3. Identifying source components – Modelling

Based on our previous discussion, the melting assemblage underlying Nyiragongo appears to be primarily composed of olivine, (clino)pyroxene, phlogopite, apatite, and minor garnet as well as possible pargasitic amphibole, with a garnet-peridotite dominated restite at a pressure >2.5 GPa. With this in mind, the experiments of Condamine *et al.* (2016, 2022) provide the closest analogues of the melting assemblage and conditions relevant to Nyiragongo. However, low degree melting batches from these experiments show significant (5-10 wt.%) compositional discrepancies when compared with lavas from this study, the most significant of which are for CaO (7 wt.% in experimental melt, 15.9 – 17.00 wt.% in parental options Mg_70, Mg_74, and Ny17-160), FeO_T (6.9 wt.% vs 10.7 – 10.8 wt.%), and SiO_2 (45.8 wt.% vs 38.0 – 38.2 wt.%).

The experiments of Lloyd *et al.* (1985) provide a more accurate match to primitive compositions erupted by Nyiragongo, and were derived from melting of an Ugandan xenolith assemblage composed of clinopyroxene (52.5%), phlogopite (35%), titanomagnetite (6.5%), titanite (4%), and apatite (2%) (Table 4). The liquids generated from 20% melting at 3 GPa were somewhat depleted

in Al_2O_3 (6.4 wt.% vs 10 – 11 wt.%) and enriched in SiO_2 (43.3 wt.% vs 38.6 – 39.1 wt.%), but otherwise match the chemical profile of Nyiragongo.

Unfortunately the experiments of Lloyd *et al.* (1985) only considered major elements, so in order to more completely address the source of Nyiragongo, we hereby apply the mantle melting modelling approach of Condamine *et al.* (2022) for 1 GPa and 3 GPa conditions, also using the partition coefficients of this study, in order to approximate a mantle source consistent with Nyiragongo magmas, including trace elements. Since no constraints on the proportions of the different phases are available, we applied the model to a variety of 10,000 randomized mantle assemblages composed of olivine, orthopyroxene, clinopyroxene, apatite, phlogopite and garnet (3 GPa), or amphibole and spinel (1 GPa). The 1 GPa run is required to assess the effect of amphibole-field melting, keeping the possibility of polybaric melting available. All mineral phases were assigned a random number between 0 and 20 (apatite, garnet, spinel, orthopyroxene) or 50 (olivine, clinopyroxene, phlogopite, amphibole), after which these were normalised to attain a total of 100%, forming the randomized mantle assemblage.

Mantle compositions matching these assemblages were calculated based on the mineral chemistries reported by Koornneef *et al.* (2009) for metasomatic intergrowths in Labait xenoliths (olivine, orthopyroxene, clinopyroxene, spinel, garnet, phlogopite), the Eifel-derived apatite compositions reported by O'Reilly and Griffin (2000), and the Eifel-derived lithospheric amphibole compositions reported by Witt-Eickschen *et al.* (2003). These can be considered the most adequate substitutes for VVP SCLM, given that Labait shares a geological history with the VVP due to its proximity, and the Eifel is a similarly alkaline continental rift setting.

Table 4 Best-fit modelling results following the modelling approach of Condamine et al. (2022) for 1 and 3 GPa and a variety of starting assemblages to best match the compositions of Mg_70, and Mg_74 (Table 3). Runs using high-Mg# and low-Mg# phlogopite are listed separately to show the effect of this change. Best-fit melt fractions (F) are included below starting assemblages. The experiment of Lloyd et al. (1985) is also included, for which sphene (4%) and Ti-magnetite (6.5%) are listed as 'others'.

Pressure	**3 GPa**	**1GPa**				**3GPa**			
		High Mg# Phl		**Low Mg# Phl**		**High Mg# Phl**		**Low Mg# Phl**	
Best fit for composition	*Lloyd et al. (1985)*	Mg_70	Mg_74	Mg_70	Mg_74	Mg_70	Mg_74	Mg_70	Mg_74
Starting assemblage									
Phl (%)	35	31.7	31.7	16.7	16.7	12.1	13.3	12.6	12.6
Opx (%)	0	6.1	6.1	11.1	11.1	0.0	11.1	0.0	0.0
Cpx (%)	52.5	11.0	11.0	14.6	14.6	52.7	54.4	46.3	46.3
Apatite (%)	2	2.4	2.4	3.5	3.5	1.1	1.1	1.1	1.1
Spinel (%)		4.9	4.9	12.5	12.5				
Garnet (%)						2.2	2.2	2.1	2.1
Olivine (%)		37.8	37.8	29.9	29.9	31.9	17.8	37.9	37.9
Amp (%)		6.1	6.1	11.8	11.8				
Others (%)	10.5								
Best-fit F (%)	*20*	*25*	*22*	*40*	*39*	*24*	*22*	*21*	*19*
wt.%									
SiO_2	*43.3*	49.9	49.2	44.2	44.0	48.8	48.3	40.6	39.3
TiO_2	*3.9*	1.3	1.5	2.3	2.3	1.2	1.2	2.2	2.4
Al_2O_3	*6.4*	6.8	7.7	7.9	8.1	6.0	6.4	6.5	7.1
FeO_T	*12.9*	3.1	3.1	4.7	4.8	3.2	3.2	5.2	5.4
MnO	*0.1*	0.1	0.1	0.1	0.1	0.3	0.3	0.3	0.3
MgO	*11.7*	13.1	11.9	9.4	9.1	17.6	17.2	12.5	11.8
CaO	*15.5*	17.8	17.7	23.9	24.1	16.9	16.8	26.8	27.6
Na_2O	*1.9*	1.8	1.9	1.6	1.6	1.4	1.4	1.1	1.0
K_2O	*3.4*	2.5	2.9	2.8	2.9	2.9	3.1	2.9	3.2
P_2O_5	*1.0*	3.5	4.0	3.0	3.1	1.8	2.0	1.8	1.9
Ppm↓									
Rb		69	72	60	61	62	64	66	69
Sr		603	660	624	638	780	849	797	859
Y		31	31	29	29	34	35	34	36
Zr		229	252	202	206	900	1000	902	987
Nb		43	47	39	40	18	21	20	23
Ba		196	200	239	242	306	340	344	370
La		125	140	114	116	75	83	80	88
Ce		333	368	303	309	224	245	236	258
Nd		124	133	114	116	111	121	115	124
Sm		21	22	20	20	21	22	21	22
Eu		4.7	4.9	4.4	4.4	5.6	5.9	5.6	5.9
Gd		13	13	12	12	15	16	15	16
Dy		2.9	2.9	2.8	2.8	7.2	7.6	7.2	7.6
Yb		2.0	2.0	1.8	1.8	2.3	2.4	2.4	2.5
Lu		0.2	0.2	0.2	0.2	0.3	0.3	0.3	0.3
Hf		8	8	6	6	24	27	24	26
Th		4.6	5.2	4.3	4.4	2.1	2.3	2.3	2.5
U		1.1	1.2	1.0	1.0	0.5	0.6	0.5	0.6
K/Rb		302	334	387	389	387	404	371	384
Rb/Sr		0.1	0.1	0.1	0.1	0.1	0.1	0.1	0.1
Ba/Rb		2.8	2.8	4.0	4.0	4.9	5.3	5.2	5.4
Th/U		4.2	4.2	4.3	4.3	4.2	4.2	4.2	4.2
$(Dy/Yb)_N$		1.0	1.0	1.0	1.0	2.1	2.1	2.0	2.0

The model uses an initial step of congruent apatite melting, after which the hydrous phases start melting incongruently. Only once these reactions are no longer feasible the model switches to incongruent melting of clinopyroxene.

Accordingly, in the 1 GPa models the hydrous phases melt incongruently following two reactions from Condamine and Médard (2014):

$$Amphibole\ breakdown\text{: } 0.39\ phlogopite + 0.49\ amphibole + 0.44\ orthopyroxene + 0.11\ clinopyroxene \rightarrow 0.49\ olivine + 1\ melt$$

$$Phlogopite - only\ melting\text{: } 0.49\ phlogopite + 0.56\ orthopyroxene + 0.47\ clinopyroxene + 0.05\ spinel \rightarrow 0.58\ olivine + 1\ melt$$

In the 3 GPa models which lack amphibole but contain garnet, phlogopite breakdown instead follows the following reaction from Condamine *et al.* (2016):

$$0.59\ phlogopite + 0.52\ clinopyroxene + 0.18\ garnet \rightarrow 0.23\ orthopyroxene + 1\ melt$$

In both models, once one of the reactants (except clinopyroxene) was consumed by the reaction, clinopyroxene melting would continue following the reaction of Sorbadere *et al.* (2013a):

$$0.11\ olivine + 0.89\ clinopyroxene \rightarrow 1\ melt$$

For each melting step of a given mantle assemblage, the resulting liquid composition was compared to compositions Mg_70 and Mg_74, after which a best-fit composition was established for that assemblage. Mismatches between calculated and target concentrations of elements/oxides were calculated on a percentage-of-target basis, while LREE (La, Ce, Nd), MREE (Sm, Eu, Gd), and HREE (Dy, Yb, Lu) were grouped and summed in order to prevent overfitting of these elements in contrast to all others. The mantle assemblages for which the best-fit melt compositions most closely approached the primitive melt analogues are listed in Table 4.

All generated compositions derived from these best-fit mantle assemblages are thoroughly depleted in FeO (3.1 – 3.2 wt.%) compared to primitive melt candidates (~10.7 wt.%), likely reflecting the specific Mg# picked for certain mineral phases. In light of this, we performed the same procedure once more, but using the more Fe-rich phlogopite major element composition of Lloyd *et al.* (1985). This increased FeO concentrations to 4.7 – 5.4 wt.%, and provided a better fit overall (Table 4), but the fact that there is still ~5 wt.% missing indicates that we may be missing an Fe-supplying phase such as the magnetite included by Lloyd *et al.* (1985).

The best-fit modelling runs best match the target compositions at melt fractions between 21 and 40% melting. This does not imply that this is the melting degree of the mantle as a whole, which would be unrealistic (e.g., Katz et al., 2003), but rather heterogeneities within it. The resulting compositions have a low Na_2O content compared to target compositions (1.0 – 1.9 wt.% vs 3.3 – 3.6. wt.%). This is especially true for the 3 GPa models since these do not involve amphibole (Table 4). Conversely, both the amphibole and clinopyroxene breakdown reactions (which consume high-Si minerals) cause melts to quickly take on SiO_2 concentrations incompatible with whole-rock observations (>44 wt.%; Fig. 8a; Table 4). Instead, because the phlogopite breakdown reaction for 3 GPa assemblages primarily consumes Si-poor phlogopite and olivine while producing SiO_2-rich orthopyroxene, it results in melts with significantly lower SiO_2 contents (Fig. 8a). The K/Rb ratios in generated melts are moderately elevated (95 – 128% of target) due to an excessive supply of K_2O during phlogopite breakdown, which is compensated for once this phase is fully consumed (Fig. 8c). Other ratios associated with amphibole and phlogopite (Rb/Sr and Ba/Rb) consistently present strong disparities between simulated and target melts, regardless of the involvement of either phase (Fig. 8e; Table 4). In contrast, garnet involvement does show a buffering effect on Dy/Yb_N ratios in 3 GPa simulations, which is lacking those without it (Fig. 8d). Individual trace elements that deviate significantly in all models include Nb (13 – 38 % of target, potentially retained by restite hydrous phases; Condamine *et al.*, 2022), Th (15 – 40% of target), and U (10 – 26% of target). The extreme LILE concentrations of Sr (624 – 859 ppm vs target 2236 – 2399 ppm) and Ba (196 – 370 ppm vs target 1172 – 1258 ppm) are also difficult to reproduce adequately, especially for 1 GPa simulations due to the Ba-poor nature of amphibole compared to phlogopite. Once the 3 GPa models run out of garnet (Fig. 8) and the melting starts to primarily break down clinopyroxene, the melt starts becoming enriched in clinopyroxene-compatible elements such as Zr (338 – 404 % of target) and Hf (457 – 540% of target). In line with the initial

617 congruent apatite melting step, we observe that many apatite-enriched trace elements (LREE, Sr,
618 Th, and U) in the melts are directly proportional to their concentrations in the starting-assemblage
619 apatite.

620 ### 5.3.1. Modelling caveats and summary of the modelling results

621 We want to emphasize that all modelling runs are subject to uncertainties resulting from a large
622 number of unknowns. Assuming the chosen assemblages and the applied melting reactions are
623 correct, further assumptions are taken with regards to the exact compositions of all phases, both in
624 trace and major element compositions, since there are no xenolith samples available from the
625 region. Lastly, two assumptions are taken during the modelling procedure: firstly, that the melting
626 reactions currently available in literature are the only ones occurring; and secondly, that the
627 partitioning behaviour during melting processes is adequately described by currently available
628 partition coefficients.
629 Nevertheless, a few key conclusions can be drawn from our modelling:
630 - Apatite (or monazite) contributions are vital to explain the phosphorous and REE
631 concentrations observed in natural samples.
632 - 3 GPa melting of a phlogopite and garnet-bearing source is in best agreement with the
633 compositions observed at Nyiragongo, primarily due to their lower SiO_2 contents, garnet-
634 buffered Dy/Yb_N ratios, and higher Ba-concentrations.
635 - Out of the 3 GPa runs the low Mg# phlogopite run with Mg_74 as its target composition
636 shows the best agreement with observations (Fig. 8).
637 - A high (20 – 40%) melting degree is expected for the low Mg# phlogopite-rich assemblage.
638 - The involvement of amphibole cannot be fully excluded, but must be minor compared to
639 that of phlogopite. Amphibole may contribute to the eventual liquid composition as melts
640 ascend towards shallower levels where this phase is stable. This may help push the Na/K
641 ratio closer towards unity.
642

643 ## 5.4. Implications for lithospheric structure

644 Both chemical proxies and modelling results favour the hypothesis of deep (≥ 3 GPa) melting of a
645 phlogopite-bearing clinopyroxenite source, with the potential of minor amphibole contributions

during ascent. However, the olivine trace element signature also indicated a peridotitic restite signature, causing a somewhat contradictory signal overall. We propose that this can be readily resolved through re-examination of the mode of emplacement of metasomatic lithologies such as clinopyroxene and phlogopite. Indeed, xenolith evidence (Dawson and Smith, 1988; Koornneef *et al.*, 2009) and conceptual models (e.g., Foley, 2008; Pilet *et al.*, 2008) infer that metasomatic phases are generally emplaced into the SCLM in the form of veins rather than completely transformed domains. If the lithosphere surrounding the veins is peridotite-dominated, the vein melts will likely re-equilibrate and lose some of their olivine-compatible trace element contents (e.g., Ni, Co) as they either pond or ascend after melting, explaining both signals (Fig. 9).

The primary reactions producing melt in our 3 GPa conceptual models are the ones of phlogopite-breakdown as described by Condamine *et al.* (2016) and clinopyroxene melting of Sorbadere *et al.* (2013) (see section 5.3). These reactions are characteristic of temperatures in the ranges of 1150 to 1350 °C and >1200 °C, respectively, corresponding narrowly to our olivine-crystallization temperatures (Fig. 6). These temperatures neither exclude nor require the presence of a plume head (directly) underlying the VVP, as is sometimes inferred (Chakrabarti *et al.*, 2009a). Indeed, these temperatures are in line with MORB- to plume-assisted MORB-settings (Herzberg *et al.*, 2007; Matthews *et al.*, 2021; Zhang *et al.*, 2023) and likely only produce volcanism in this region due to the presence of these hydrous metasomatic veins. The melting of the veins may be triggered in response to local crustal extension or thermal perturbations by an underlying, or regionally influential plume. This agrees with the mixed plume-SCLM isotope signature reported by Halldórsson *et al.* (2014) for this part of the rift. Indeed, the preferential melting of K-rich vein material in the western rift in general is in line with the anomalously K-rich lavas that are erupted here, contrasting with the more Na-rich volcanism in the eastern branch (Foley *et al.*, 2012).

Three possible reasons for this discrepancy can be proposed:

1) Higher degrees of melting in the eastern branch, as is generally observed through its more voluminous deposits (Chorowicz, 2005), would cause more of the non-metasomatic domains to be molten, diluting their K-rich signature.
2) Vein materials in this region may have already been depleted due to the higher magma supply.
3) The SCLM underlying the eastern branch has undergone (locally) different degrees/ types of metasomatism.

We argue for a combination of explanations 1 and 3, given the clear evidence for metasomatized mantle domains in the region (Dawson and Smith, 1992; Koornneef *et al.*, 2009), and the fact that exotic, K-rich magmas are still locally erupted here. In the southern lying Rungwe province, similarly Na-rich, silica-undersaturated lavas are explained through lithospheric amphibole (Furman, 1995), but local variations in silica-undersaturation are explained through variable degrees of melting.

The hydrated veins under Nyiragongo are most likely emplaced by low-degree melts resulting from either lithospheric erosion (Furman and Graham, 1999; Foley, 2008), or slab melting during late Pan-African subduction (Vollmer and Norry, 1983a; Pitcavage *et al.*, 2021). Due to their hydrated nature, veins melt more readily than the surrounding mantle, enriching the produced magma in their chemical constituents (Ca, alkalis, LILE). Mantle-to-surface ascent rates for Nyiragongo were estimated by Chakrabarti *et al.* (2009b) to be in the order of 8 ka, which is sufficient to permit significant elemental diffusion between lithosphere and melt, especially for highly diffusive transition metals (Spandler and O'Neill, 2010).

It follows that whereas our results provide useful insights into the mantle melting beneath Nyiragongo, they also highlight the complexity of the region's magmatic processes, in which heterogeneous metasomatic domains and variations in melting depths, heat fluxes, and consequential degrees of melting produce a highly diverse suite of volcanic systems and eruptive products. Additional experimental investigations on possible melting reactions and mantle assemblages in metasomatised mantle domains may help further elucidate the exact mineral composition of the source under Nyiragongo.

6. CONCLUSIONS

Evaluating primitive whole-rock and olivine compositions indicates that the primitive melts of Nyiragongo are not represented among erupted lavas, but are compositionally in between the OMB- and PMB-types described by Molendijk *et al.* (2024). High LREE and LILE concentrations as well as positive K/Na ratios indicate that these melts are derived from incongruent melting of phlogopite, clinopyroxene, apatite, and garnet. This melting is inferred to occur at pressures beyond ~3 GPa, in a veined, metasomatized lithosphere underlying the larger VVP. Due to the highly localised nature of metasomatic veins, we observe opposing signals from whole-rock and olivine trace element compositions, the former suggesting a pyroxenite source and the latter suggesting a peridotite source. This apparent contradiction likely reflects melting of hydrous

pyroxenite veins followed by re-equilibration of melts with volumetrically dominant olivine-rich lithospheric mantle. Mantle melting models indicate that major amphibole involvement in the source assemblage of Nyiragongo is unlikely, given that the melting thereof would produce SiO_2 concentrations greater than those observed. The conditions at which the vein-melting reactions take place suggest MORB-like mantle temperatures and minimal heat loss prior to early olivine crystallization, without the explicit need for a plume head underlying the region, though one could be contributing to a thermal perturbation in the system. The localized, vein-dominated nature of these melting processes causes the distinctly K-rich, Si-undersaturated signature of Nyiragongo lavas, contrasting the more Na-rich, more Si-saturated volcanism generated by higher degrees of melting in other regions of the rift.

Acknowledgements

The authors would like to acknowledge Zoë van Beeck for her assistance in the mounting and analysis of olivine crystals. We are also grateful to Eric Hellebrand of the microprobe facility at Utrecht University for his assistance with EPMA analyses. We would like to extend our thanks to two anonymous reviewers who helped improve the manuscript in its final stages.

References

Aiuppa, A., Casetta, F., Coltorti, M., Stagno, V. & Tamburello, G. (2021). Carbon concentration increases with depth of melting in Earth's upper mantle. *Nature Geoscience*. Springer US **14**, 697–703.

Altherr, R., Henjes-Kunst, F., Puchelt, H. & Baumann, A. (1988). Volcanic activity in the Red Sea axial trough - evidence for a large mantle diapir? *Tectonophysics* **150**, 121–133.

Ammannati, E., Jacob, D. E., Avanzinelli, R., Foley, S. F. & Conticelli, S. (2016). Low Ni olivine in silica-undersaturated ultrapotassic igneous rocks as evidence for carbonate metasomatism in the mantle. *Earth and Planetary Science Letters*. Elsevier B.V. **444**, 64–74.

Baptiste, V., Tommasi, A., Vauchez, A., Demouchy, S. & Rudnick, R. L. (2015). Deformation, hydration, and anisotropy of the lithospheric mantle in an active rift: Constraints from mantle xenoliths from the North Tanzanian Divergence of the East African Rift. *Tectonophysics*. Elsevier B.V. **639**, 34–55.

Barette, F., Poppe, S., Smets, B., Benbakkar, M. & Kervyn, M. (2017). Spatial variation of

volcanic rock geochemistry in the Virunga Volcanic Province: Statistical analysis of an integrated database. *Journal of African Earth Sciences*. Elsevier Ltd **134**, 888–903.

Barker, A. K., Holm, P. M. & Troll, V. M. (2014). The role of eclogite in the mantle heterogeneity at Cape Verde. *Contributions to Mineralogy and Petrology* **168**, 1–15.

Batanova, V. G. *et al.* (2019). New Olivine Reference Material for In Situ Microanalysis. *Geostandards and Geoanalytical Research* **43**, 453–473.

Baudouin, C. & Parat, F. (2020). Phlogopite-Olivine Nephelinites Erupted During Early Stage Rifting, North Tanzanian Divergence. *Frontiers in Earth Science* **8**, 1–22.

Bedini, R. M., Bodinier, J.-L., Dautria, J.-M. & Morten, L. (1997). Evolution of LILE-enriched small melt fractions in the lithospheric mantle: a case study from the East African Rift. *Earth and Planetary Science Letters* **153**.

Bell, K. & Powell, J. L. (1969). Strontium isotopic studies of alkalic rocks: The potassium-rich lavas of the birunga and toro - ankole regions, east and central equatorial Africa. *Journal of Petrology* **10**, 536–572.

Bracco, A. J. J., Nikogosian, I. K., Davies, G. R. & Koornneef, J. M. (2023). The multi-component mantle source of Roman province ultrapotassic magmas revealed by melt inclusions. *Geochimica et Cosmochimica Acta*. Elsevier Ltd **355**, 266–281.

Bultitude, R. J. & Green, D. H. (1971). Experimental study of crystal-liquid relationships at high pressures in olivine nephelinite and basanite compositions. *Journal of Petrology* **12**, 121–147.

Caldwell, D. A. & Kyle, P. R. (1994). Mineralogy and Geochemistry of Ejecta erupted from Mount Erebus, Antarctica, Between 1972 and 1986. *Volcanological and Environmental Studies of Mount Erebus, Antarctica*, 147–162.

Castillo, P. R., Hilton, D. R. & Halldórsson, S. A. (2014). Trace element and Sr-Nd-Pb isotope geochemistry of Rungwe Volcanic Province, Tanzania: implications for a Superplume source for East Africa Rift magmatism. *Frontiers in Earth Science* **2**, 1–17.

Chakrabarti, R., Basu, A. R., Santo, A. P., Tedesco, D. & Vaselli, O. (2009a). Isotopic and geochemical evidence for a heterogeneous mantle plume origin of the Virunga volcanics, Western rift, East African Rift system. *Chemical Geology*. Elsevier B.V. **259**, 273–289.

Chakrabarti, R., Sims, K. W. W., Basu, A. R., Reagan, M. & Durieux, J. (2009b). Timescales of magmatic processes and eruption ages of the Nyiragongo volcanics from 238U-230Th-

226Ra-210Pb disequilibria. *Earth and Planetary Science Letters*. Elsevier B.V. **288**, 149–157.

Chorowicz, J. (2005). The East African rift system. *Journal of African Earth Sciences* **43**, 379–410.

Class, C. & Goldstein, S. L. (1997). Plume-lithosphere interactions in the ocean basins: constraints from the source mineralogy. *Earth and Planetary Science Letters* **150**, 245–260.

Coltorti, M., Bonadiman, C., Faccini, B., Grégoire, M., O'Reilly, S. Y. & Powell, W. (2007). Amphiboles from suprasubduction and intraplate lithospheric mantle. *Lithos* **99**, 68–84.

Conceiçao, R. V. & Green, D. H. (2004). Derivation of potassic (shoshonitic) magmas by decompression melting of phlogopite+pargasite lherzolite. *Lithos* **72**, 209–229.

Condamine, P., Couzinie, S., Fabbrizio, A., Devidal, J. & Médard, E. (2022). Trace element partitioning during incipient melting of phlogopite-peridotite in the spinel and garnet stability fields. *Geochimica et Cosmochimica Acta* **327**, 53–78.

Condamine, P. & Médard, E. (2014). Experimental melting of phlogopite-bearing mantle at 1 GPa: Implications for potassic magmatism. *Earth and Planetary Science Letters*. Elsevier B.V. **397**, 80–92.

Condamine, P., Médard, E. & Luc, J. (2016). Experimental melting of phlogopite - peridotite in the garnet stability field. *Contributions to Mineralogy and Petrology*. Springer Berlin Heidelberg **171**, 1–26.

Condomines, M., Carpentier, M. & Ongendangenda, T. (2015). Extreme radium deficit in the 1957 AD Mugogo lava (Virunga volcanic field, Africa): its bearing on olivine-melilitite genesis. *Contributions to Mineralogy and Petrology* **169**, 1–19.

Davidson, J., Turner, S. & Plank, T. (2013). Dy/Dy*: Variations arising from mantle sources and petrogenetic processes. *Journal of Petrology* **54**, 525–537.

Dawson, J. B. & Smith, J. V. (1988). Metasomatised and veined upper-mantle xenoliths from Pello Hill, Tanzania: evidence for anomalously-light mantle beneath the Tanzanian sector of the East African Rift Valley. *Contributions to Mineralogy and Petrology* **100**, 510–527.

Dawson, J. B. & Smith, J. V. (1992). Olivine-mica pyroxenite xenoliths from northern Tanzania: metasomatic products of upper-mantle peridotite. *Journal of Volcanology and Geothermal Research* **50**, 131–142.

Dawson, J. B., Smith, J. V. & Steele, I. M. (1994). Trace-element distribution between

coexisting perovskite, apatite and titanite from Oldoinyo Lengai, Tanzania. *Chemical Geology* **117**, 285–290.

Dawson, J. B., Smith, J. V. & Steele, I. M. (1995). Petrology and Mineral Chemistry of Plutonic Igneous Xenoliths from the Carbonatite Volcano, Oldoinyo Lengai, Tanzania. *Journal of Petrology* **36**, 797–826.

Demant, A., Lestrade, P., Lubala, R. T., Kampunzu, A. B. & Durieux, J. (1994). Volcanological and petrological evolution of Nyiragongo volcano, Virunga volcanic field, Zaire. *Bulletin of Volcanology* **56**, 47–61.

Droop, G. T. R. (1987). A general equation for estimating Fe3+ concentrations in ferromagnesian silicates and oxides from microprobe analyses , using stoichiometric criteria. *Mineralogical Magazine* **51**, 431–435.

Dupuy, C., Liotard, J. M. & Dostal, J. (1992). Zr/Hf fractionation in intraplate basaltic rocks: Carbonate metasomatism in the mantle source. *Geochimica et Cosmochimica Acta* **56**, 2417–2423.

Ebinger, C. J. (1989). Tectonic development of the western branch of the East African rift system. *Geological Society Of America Bulletin* **101**, 885–903.

Ebinger, C. J. & Furman, T. (2003). Geodynamical Setting of the Virunga Volcanic Province. *Acta Vulcanologica* **14**, 1–8.

Ebinger, C. J. & Sleep, N. H. (1998). Cenozoic magmatism throughout east Africa resulting from impact of a single plume. *Nature* **395**, 788–791.

Eby, G. N., Lloyd, F. E., Woolley, A. R., Stoppa, F. & Weaver, S. D. (2003). Geochemistry and mantle source(s) for carbonatititic and potassic lavas, Western branch of the East-African Rift System, SW Uganda. *GeoLines* **15**, 23–27.

Fitton, J. G. (2008). The Cameroon line, West Africa: a comparison between oceanic and continental alkaline volcanism. *Geological Society, London, Special Publications* **30**, 273–291.

Foley, S. (1992). Vein-plus-wall-rock melting mechanisms in the lithosphere and the origin of potassic alkaline magmas. *Lithos* **28**, 435–453.

Foley, S. F. (2008). Rejuvenation and erosion of the cratonic lithosphere. *Nature Geoscience* **1**, 503–510.

Foley, S. F. & Fischer, T. P. (2017). An essential role for continental rifts and lithosphere in the

deep carbon cycle. *Nature Geoscience*. Springer US **10**.

Foley, S. F., Jacob, D. E. & O'Neill, H. S. C. (2011). Trace element variations in olivine phenocrysts from Ugandan potassic rocks as clues to the chemical characteristics of parental magmas. *Contributions to Mineralogy and Petrology* **162**, 1–20.

Foley, S. F., Link, K., Tiberindwa, J. V. & Barifaijo, E. (2012). Patterns and origin of igneous activity around the Tanzanian craton. *Journal of African Earth Sciences*. Elsevier Ltd **62**, 1–18.

Foley, S. F., Prelevic, D., Rehfeldt, T. & Jacob, D. E. (2013). Minor and trace elements in olivines as probes into early igneous and mantle melting processes. *Earth and Planetary Science Letters*. Elsevier **363**, 181–191.

Fontijn, K., Williamson, D., Mbede, E. & Ernst, G. G. J. (2012). The Rungwe Volcanic Province, Tanzania - A volcanological review. *Journal of African Earth Sciences*. Elsevier Ltd **63**, 12–31.

Freestone, I. C. & Hamilton, D. L. (1980). The role of liquid immiscibility in the genesis of carbonatites - An experimental study. *Contributions to Mineralogy and Petrology* **73**, 105–117.

Furman, T. (1995). Melting of metasomatized subcontinental lithosphere: undersaturated mafic lavas from Rungwe , Tanzania. *Contributions to Mineralogy and Petrology* **122**, 97–115.

Furman, T. & Graham, D. (1999). Erosion of lithospheric mantle beneath the East African Rift system: geochemical evidence from the Kivu volcanic province. *Lithos* **48**, 237–262.

Furman, T., Kaleta, K. M., Bryce, J. G. & Hanan, B. B. (2006). Tertiary mafic lavas of Turkana, Kenya: Constraints on East African plume structure and the occurrence of high-μ volcanism in Africa. *Journal of Petrology* **47**, 1221–1244.

Furman, T., Nelson, W. R. & Elkins-Tanton, L. T. (2015). Evolution of the East African rift: Drip magmatism, lithospheric thinning and mafic volcanism. *Geochimica et Cosmochimica Acta*. Elsevier Ltd **185**, 418–434.

Gee, L. L. & Sack, R. O. (1988). Experimental petrology of melilite nephelinites. *Journal of Petrology* **29**, 1233–1255.

Gibson, S. A., McMahon, S. C., Day, J. A. & Dawson, J. B. (2013). Highly refractory lithospheric mantle beneath the tanzanian craton: Evidence from lashaine pre-metasomatic garnet-bearing peridotites. *Journal of Petrology* **54**, 1503–1546.

862 Gleeson, M. L. M. & Gibson, S. A. (2019). Crustal controls on apparent mantle pyroxenite
863 signals in ocean-island basalts. *Geology* **47**, 321–324.
864 Green, D. H. & Falloon, T. J. (1998). Pyrolite: a Ringwood concept and its current expression.
865 In: Jackson, I. N. S. (ed.) *The Earth's Mantle: Composition, Structure, and Evolution*. New
866 York: Cambridge University Press, 311–380.
867 Grijalva, A. *et al.* (2018). Seismic Evidence for Plume- and Craton-Influenced Upper Mantle
868 Structure Beneath the Northern Malawi Rift and the Rungwe Volcanic Province, East
869 Africa. *Geochemistry, Geophysics, Geosystems* **19**, 3980–3994.
870 Haase, K. M., Mühe, R. & Stoffers, P. (2000). Magmatism during extension of the lithosphere:
871 Geochemical constraints from lavas of the Shaban Deep, northern Red Sea. *Chemical*
872 *Geology* **166**, 225–239.
873 Halldórsson, S. A., Hilton, D. R., Scarsi, P., Abebe, T. & Hopp, J. (2014). A common mantle
874 plume source beneath the entire East African Rift System revealed by coupled helium-neon
875 systematics. *Geophysical Research Letters* **41**, 2304–2311.
876 Hauri, E. H., Wagner, T. P. & Grove, T. L. (1994). Experimental and natural partitioning of Th,
877 U, Pb and other trace elements between garnet, clinopyroxene and basaltic melts. *Chemical*
878 *Geology* **117**, 149–166.
879 Head, E. M., Lanzirotti, A., Newville, M. & Sutton, S. (2018). Vanadium, sulfur, and iron
880 valences in melt inclusions as a window into magmatic processes: A case study at
881 Nyamuragira volcano, Africa. *Geochimica et Cosmochimica Acta*. Elsevier Ltd **226**, 149–
882 173.
883 Heinonen, J. S., Luttinen, A. V & Bohrson, W. A. (2016). Enriched continental flood basalts
884 from depleted mantle melts: modeling the lithospheric contamination of Karoo lavas from
885 Antarctica. *Contributions to Mineralogy and Petrology*. Springer Berlin Heidelberg **171**, 1–
886 22.
887 Hertogen, J., Vanlerberghe, L. & Namegabe, M. R. (1985). Geochemical evolution of the
888 Nyiragongo volcano (Virunga, Western African Rift, Zaire). *Bulletin of the Geological*
889 *Society of Finland* **57**, 21–35.
890 Herzberg, C. (2006). Petrology and thermal structure of the Hawaiian plume from Mauna Kea
891 volcano. *Nature* **444**, 605–609.
892 Herzberg, C., Asimow, P. D., Arndt, N. T., Niu, Y., Lesher, C. M., Fitton, J. G., Cheadle, M. J.

& Saunders, A. D. (2007). Temperatures in ambient mantle and plumes: Constraints from basalts, picrites, and komatiites. *Geochemistry, Geophysics, Geosystems* **8**.

Hilton, D. R., Halldórsson, S. A., Barry, P. H., Fischer, T. P., De Moor, J. M., Ramirez, C. J., Mangasini, F. & Scarsi, P. (2011). Helium isotopes at Rungwe Volcanic Province, Tanzania, and the origin of East African Plateaux. *Geophysical Research Letters* **38**, 1–5.

Howarth, G. H. & Harris, C. (2017). Discriminating between pyroxenite and peridotite sources for continental flood basalts (CFB) in southern Africa using olivine chemistry. *Earth and Planetary Science Letters*. Elsevier B.V. **475**, 143–151.

Innocenzi, F., Ronca, S., Foley, S., Agostini, S. & Lustrino, M. (2024). Carbonatite and ultrabasic magmatism at Toro Ankole and Virunga , western branch of the East African Rift system. *Gondwana Research*. The Author(s) **125**, 317–342.

Keller, J., Zaitsev, A. N. & Wiedenmann, D. (2006). Primary magmas at Oldoinyo Lengai: The role of olivine melilitites. *Lithos* **91**, 150–172.

Klaudius, J. & Keller, J. (2006). Peralkaline silicate lavas at Oldoinyo Lengai, Tanzania. *Lithos* **91**, 173–190.

Klemme, S. & O'Neill, H. S. C. (2000). The near-solidus transition from garnet lherzolite to spinel lherzolite. *Contributions to Mineralogy and Petrology* **138**, 237–248.

Koornneef, J. M., Davies, G. R., Döpp, S. P., Vukmanovic, Z., Nikogosian, I. K. & Mason, P. R. D. (2009). Nature and timing of multiple metasomatic events in the sub-cratonic lithosphere beneath Labait, Tanzania. *Lithos*. Elsevier B.V. **1125**, 896–912.

Kress, V. C. & Carmichael, I. S. E. (1991). The compressibility of silicate liquids containing Fe2O3 and the effect of composition, temperature, oxygen fugacity and pressure on their redox states. *Contributions to Mineralogy and Petrology* **108**, 82–92.

Lambart, S., Laporte, D. & Schiano, P. (2009). An experimental study of pyroxenite partial melts at 1 and 1.5 GPa: Implications for the major-element composition of Mid-Ocean Ridge Basalts. *Earth and Planetary Science Letters*. Elsevier B.V. **288**, 335–347.

Lambart, S., Laporte, D. & Schiano, P. (2013). Markers of the pyroxenite contribution in the major-element compositions of oceanic basalts: Review of the experimental constraints. *Lithos*. Elsevier B.V. **160**–**161**, 14–36.

LaTourrette, T., Hervig, R. L. & Holloway, J. R. (1995). Trace element partitioning between amphibole, phlogopite, and basanite melt. *Earth and Planetary Science Letters* **135**, 13–30.

924 Lloyd, F. E. (1981). Upper-mantle metasomatism beneath a continental rift: clinopyroxenes in
925 alkali mafic lavas and nodules from South West Uganda. *Mineralogical Magazine* **44**, 315–
926 323.
927 Lloyd, F. E. (1985). Experimental melting and crystallisation of glassy olivine melilitites.
928 *Contributions to Mineralogy and Petrology* **90**, 236–243.
929 Lloyd, F. E., Arima, M. & Edgar, A. D. (1985). Partial melting of a phlogopite-clinopyroxenite
930 nodule from south-west Uganda: an experimental study bearing on the origin of highly
931 potassic continental rift volcanics. *Contributions to Mineralogy and Petrology* **91**, 321–329.
932 Marcelot, G. & Rançon, J. P. (1988). Mineral Chemistry of Leucitites from Visoke Volcano
933 (Virunga Range, Rwanda): Petrogenetic Implications. *Mineralogical Magazine* **52**, 603–
934 613.
935 Marks, M., Halama, R., Wenzel, T. & Markl, G. (2004). Trace element variations in
936 clinopyroxene and amphibole from alkaline to peralkaline syenites and granites:
937 Implications for mineral-melt trace-element partitioning. *Chemical Geology* **211**, 185–215.
938 Martin, A. P., Cooper, A. F. & Dunlap, W. J. (2010). Geochronology of Mount Morning,
939 Antarctica: Two-phase evolution of a long-lived trachyte-basanite-phonolite eruptive center.
940 *Bulletin of Volcanology* **72**, 357–371.
941 Matthews, S., Wong, K., Shorttle, O., Edmonds, M. & Maclennan, J. (2021). Do olivine
942 crystallization temperatures faithfully record mantle temperature variability? *Geochemistry
943 Geophysics Geosystems* 1–42.
944 Matzen, A. K., Baker, M. B., Beckett, J. R. & Stolper, E. M. (2013). The temperature and
945 pressure dependence of nickel partitioning between olivine and silicate melt. *Journal of
946 Petrology* **54**, 2521–2545.
947 Matzen, A. K., Baker, M. B., Beckett, J. R., Wood, B. J. & Stolper, E. M. (2017a). The effect of
948 liquid composition on the partitioning of Ni between olivine and silicate melt. *Contributions
949 to Mineralogy and Petrology*. Springer Berlin Heidelberg **172**, 1–18.
950 Matzen, A. K., Wood, B. J., Baker, M. B. & Stolper, E. M. (2017b). The roles of pyroxenite and
951 peridotite in the mantle sources of oceanic basalts. *Nature Geoscience* **10**, 530–535.
952 McConnel, R. B. (1972). Geological development of the rift system of eastern Africa. *Geological
953 Society of America Bulletin* **83**, 2549–2572.
954 Médard, E., Schmidt, M. W., Schiano, P. & Ottolini, L. (2006). Melting of amphibole-bearing

wehrlites: An experimental study on the origin of ultra-calcic nepheline-normative melts. *Journal of Petrology* **47**, 481–504.

Minissale, S., Casalini, M., Cucciniello, C., Balagizi, C., Tedesco, D., Boudoire, G., Morra, V. & Melluso, L. (2022). The geochemistry of recent Nyamulagira and Nyiragongo potassic lavas, Virunga Volcanic Province, and implications on the enrichment processes in the mantle lithosphere of the Tanzania-Congo craton. *Lithos*. Elsevier B.V. **420**–**421**, 106696.

Minissale, S., Zanetti, A., Tedesco, D., Morra, V. & Melluso, L. (2019). The petrology and geochemistry of Nyiragongo lavas of 2002, 2016, 1977 and 2017 AD, and the trace element partitioning between melilitite glass and melilite, nepheline, leucite, clinopyroxene, apatite, olivine and Fe-Ti oxides: a unique scenario. *Lithos*. Elsevier B.V. **332**–**333**, 296–311.

Molendijk, S. M., Namur, O., Kaleghetso, E. K., Mason, P. R. D., Smets, B., Vander Auwera, J. & Neave, D. A. (2024). Plumbing system architecture and differentiation processes of the Nyiragongo volcano, DR Congo. *Journal of Petrology* **65**, 1–34.

Molendijk, S. M., Namur, O., Mason, P. R. D., Dubacq, B., Smets, B., Neave, D. A. & Charlier, B. (2023). Trace element partitioning in silica-undersaturated alkaline magmatic systems. *Geochimica et Cosmochimica Acta* **346**, 29–53.

Mollex, G., Füri, E., Burnard, P., Zimmermann, L., Chazot, G., Kazimoto, E. O., Marty, B. & France, L. (2018). Tracing helium isotope compositions from mantle source to fumaroles at Oldoinyo Lengai volcano , Tanzania. *Chemical Geology*. Elsevier **480**, 66–74.

Moore, J. A. & Kyle, P. R. (1987). Volcanic Geology of Mount Erebus, Ross Island, Antarctica. *Proceedings of the NIPR Symposium on Antarctic Geosciences* **1**, 48–65.

Muravyeva, N. S., Belyatsky, B. V, Senin, V. G. & Ivanov, A. V (2014). Sr – Nd – Pb isotope systematics and clinopyroxene-host disequilibrium in ultra-potassic magmas from Toro-Ankole and Virunga , East-African Rift : Implications for magma mixing and source heterogeneity. *Lithos*. Elsevier B.V. **210**–**211**, 260–277.

Muravyeva, N. S. & Senin, V. G. (2016). Glimmerite-Wehrlite Xenolith from the Ugandite of East African Rift : Mineral Composition and Conditions of Formation. *Geochemistry International* **54**, 457–463.

Muravyeva, N. S. & Senin, V. G. (2018). Xenoliths from Bunyaruguru volcanic field: Some insights into lithology of East African Rift upper mantle. *LITHOS*. Elsevier B.V. **296**–**299**, 17–36.

Muravyeva, N. S., Senin, V. G., Ivanov, A. V & Belyatsky, B. V (2021). Leucite basanites of Virunga (East African Rift): some insights into petrogenesis and source composition. *Lithos*. Elsevier B.V. **384**–**385**, 1–25.

Mysen, B. O. (1979). Nickel partitioning between olivine and silicate melt: Henry's law revisited. *American Mineralogist* **64**, 1107–1114.

Neave, D. A., Shorttle, O., Oeser, M., Weyer, S. & Kobayashi, K. (2018). Mantle-derived trace element variability in olivines and their melt inclusions. *Earth and Planetary Science Letters*. Elsevier B.V. **483**, 90–104.

Nelson, W. R., Hanan, B. B., Graham, D. W., Shirey, S. B., Yirgu, G., Ayalew, D. & Furman, T. (2019). Distinguishing Plume and Metasomatized Lithospheric Mantle Contributions to Post-Flood Basalt Volcanism on the Southeastern Ethiopian Plateau. *Journal of Petrology* **60**, 1063–1094.

Niida, K. & Green, H. (1999). Stability and chemical composition of pargasitic amphibole in MORB pyrolite under upper mantle conditions. *Contributions to Mineralogy and Petrology* **135**, 18–40.

Nikogosian, I. K. & van Bergen, M. J. (2010). Heterogeneous mantle sources of potassium-rich magmas in central-southern Italy: Melt inclusion evidence from Roccamonfina and Ernici (Mid Latina Valley). *Journal of Volcanology and Geothermal Research*. Elsevier B.V. **197**, 279–302.

Njinju, E. A., Stamps, D. S., Neumiller, K. & Gallager, J. (2021). Lithospheric Control of Melt Generation Beneath the Rungwe Volcanic Province, East Africa: Implications for a Plume Source. *Journal of Geophysical Research: Solid Earth* **126**.

Nyblade, A. A. & Brazier, R. A. (2002). Precambrian lithospheric controls on the development of the East African rift system. *Geology* **30**, 755–758.

O'Reilly, S. Y. & Griffin, W. L. (2000). Apatite in the mantle: Implications for metasomatic processes and high heat production in Phanerozoic mantle. *Lithos* **53**, 217–232.

Peterson, T. D. (1990). Petrology and genesis of natrocarbonatite. *Contributions to Mineralogy and Petrology* **105**, 143–155.

Pik, R., Marty, B. & Hilton, D. R. (2006). How many mantle plumes in Africa? The geochemical point of view. *Chemical Geology* **226**, 100–114.

Pilet, S., Baker, M. B. & Stolper, E. M. (2008). Metasomatized Lithosphere and the Origin of

Alkaline Lavas. *Science* **320**, 916–919.

Pitcavage, E., Furman, T., Nelson, W. R., Graham, D. W., Shirey, S. & Kulyanyingi, P. K. (2023). Geochemical Constraints on the Origin of Primitive Potassic Lavas in the Eastern Virunga Volcanic Province. *Geochemistry , Geophysics , Geosystems* 1–18.

Pitcavage, E., Furman, T., Nelson, W. R., Kalegga, P. K. & Barifaijo, E. (2021). Petrogenesis of primitive lavas from the Toro Ankole and Virunga Volcanic Provinces : Metasomatic mineralogy beneath East Africa's Western Rift. *Lithos*. Elsevier B.V. **396**–**397**.

Platz, T., Foley, S. F. & André, L. (2004). Low-pressure fractionation of the Nyiragongo volcanic rocks, Virunga Province, D.R. Congo. *Journal of Volcanology and Geothermal Research* **136**, 269–295.

Pouclet, A., Bellon, H. & Bram, K. (2016). The Cenozoic volcanism in the Kivu rift: Assessment of the tectonic setting, geochemistry, and geochronology of the volcanic activity in the South-Kivu and Virunga regions. *Journal of African Earth Sciences*. Elsevier Ltd **121**, 219–246.

Roberts, E. M., Stevens, N. J., O'Connor, P. M., Dirks, P. H. G. M., Gottfried, M. D., Clyde, W. C., Armstrong, R. A., Kemp, A. I. S. & Hemming, S. (2012). Initiation of the western branch of the East African Rift coeval with the eastern branch. *Nature Geoscience*. Nature Publishing Group **5**, 289–294.

Robinson, J. A. C. & Wood, B. J. (1998). The depth of the spinel to garnet transition at the peridotite solidus. *Earth and Planetary Science Letters* **164**, 277–284.

Rosenthal, A., Foley, S. F., Pearson, D. . G., Nowell, G. . M. & Tappe, S. (2009). Petrogenesis of strongly alkaline primitive volcanic rocks at the propagating tip of the western branch of the East African Rift. *Earth and Planetary Science Letters*. Elsevier B.V. **284**, 236–248.

Rudnick, R. L., Mcdonough, W. F. & Chappell, B. W. (1993). Carbonatite metasomatism in the northern Tanzanian mantle: petrographic and geochemical characteristics. *Earth and Planetary Science Letters* **114**, 463–475.

Sahama, T. G. (1962). Petrology of Mt. Nyiragongo: a review. *Transactions of the Edinburgh Geological Society* **19**, 1–28.

Sahama, T. G. (1978). The Nyiragongo main cone. *Musée royale de l'Afrique centrale - Tervuren Belgique: Annales - Série in -8°, Sciences Géologiques* **81**, 88.

Sahama, T. G. & Meyer, A. (1958). *Study of the volcano Nyiragongo. A progress report.*

Exploration du Parc National Albert. Mission d'études volcanologiques. Fascicule 2. .

Salters, V. J. M. & Longhi, J. (1999). Trace element partitioning during the initial stages of melting beneath mid-ocean ridges. *Earth and Planetary Science Letters* **166**, 15–30.

Sobolev, A. V. *et al.* (2007). The amount of recycled crust in sources of mantle-derived melts. *Science* **316**, 412–417.

Sobolev, A. V., Hofmann, A. W., Sobolev, S. V. & Nikogosian, I. K. (2005). An olivine-free mantle source of Hawaiian shield basalts. *Nature* **434**, 590–597.

Sorbadere, F., Médard, E., Laporte, D. & Schiano, P. (2013a). Experimental melting of hydrous peridotite-pyroxenite mixed sources: Constraints on the genesis of silica-undersaturated magmas beneath volcanic arcs. *Earth and Planetary Science Letters*. Elsevier B.V. **384**, 42–56.

Sorbadere, F., Schiano, P. & Métrich, N. (2013b). Constraints on the origin of nepheline-normative primitive magmas in Island arcs inferred from olivine-hosted melt inclusion compositions. *Journal of Petrology* **54**, 215–233.

Spandler, C. & O'Neill, H. S. C. (2010). Diffusion and partition coefficients of minor and trace elements in San Carlos olivine at 1,300°C with some geochemical implications. *Contributions to Mineralogy and Petrology* **159**, 791–818.

Stamps, D. S., Calais, E., Saria, E., Hartnady, C., Nocquet, J., Ebinger, C. J. & Fernandes, R. M. (2008). A kinematic model for the East African Rift. *Geophysical Research Letters* **35**, 1–6.

Sun, S. -s. & McDonough, W. F. (1989). Chemical and isotopic systematics of oceanic basalts: implications for mantle composition and processes. *Geological Society, London, Special Publications* **42**, 313–345.

Toplis, M. J. (2005). The thermodynamics of iron and magnesium partitioning between olivine and liquid: Criteria for assessing and predicting equilibrium in natural and experimental systems. *Contributions to Mineralogy and Petrology* **149**, 22–39.

Toscani, L., Capedri, S. & Oddone, M. (1990). New chemical and petrographic data of some undersaturated lavas from Nyiragongo and Mikeno (Virunga - Western African Rift - Zaire). *Neues Jahrbuch für Mineralogie - Abhandlungen* **161**, 287–302.

Veksler, I. V, Dorfman, A. M., Dulski, P., Kamenetsky, V. S., Danyushevsky, L. V, Jeffries, T. & Dingwell, D. B. (2012). Partitioning of elements between silicate melt and immiscible fluoride , chloride, carbonate, phosphate and sulfate melts, with implications to the origin of

natrocarbonatite. *Geochimica et Cosmochimica Acta*. Elsevier Ltd **79**, 20–40.

Veter, M., Foley, S. F., Mertz-kraus, R. & Groschopf, N. (2017). Trace elements in olivine of ultramafic lamprophyres controlled by phlogopite-rich mineral assemblages in the mantle source. *Lithos*. Elsevier B.V. **292**–**293**, 81–95.

Vollmer, R. & Norry, M. J. (1983a). Unusual isotopic variations in Nyiragongo nephelinites. *Nature* **301**, 141–143.

Vollmer, R. & Norry, M. J. (1983b). Possible origin of K-rich volcanic rocks from Virunga, East Africa, by metasomatism of continental crustal material: Pb , Nd and Sr isotopic evidence. *Earth and Planetary Science Letters* **64**, 374–386.

Vozniak, A. A., Kopylova, M. G., Peresetskaya, E. V, Nosova, A. A. & Sazonova, L. V (2023). Olivine in lamprophyres of the Kola Alkaline Province and the magmatic evolution of olivine in carbonate melts. *Lithos*. Elsevier B.V. **448**–**449**.

Williams, R. W. & Gill, J. B. (1992). TH isotope and U-series disequilibria in some alkali basalts. *Geophysical Research Letters* **19**, 139–142.

Witt-Eickschen, G., Seck, H. A., Mezger, K., Eggins, S. M. & Altherr, R. (2003). Lithospheric mantle evolution beneath the Eifel (Germany): Constraints from Sr-Nd-Pb isotopes and trace element abundances in spinel peridotite and pyroxenite xenoliths. *Journal of Petrology* **44**, 1077–1095.

Wong, K., Ferguson, D., Matthews, S., Morgan, D., Zafu, A., Sinetebeb, Y. & Yirgu, G. (2022). Exploring rift geodynamics in Ethiopia through olivine-spinel Al-exchange thermometry and rare-earth element distributions. *Earth and Planetary Science Letters*. Elsevier B.V. **597**, 117820.

Yaxley, G. M. & Green, D. H. (1998). Reactions between eclogite and peridotite: Mantle refertilisation by subduction of oceanic crust. *Schweiz. Mineral. Petrogr. Mitt.* **78**, 243–255.

Zhang, Y., Namur, O., Li, W., Shorttle, O., Gazel, E., Jennings, E., Thy, P., Grove, T. L. & Charlier, B. (2023). An Extended Calibration of the Olivine – Spinel Aluminum Exchange Thermometer : Application to the Melting Conditions and Mantle Lithologies of Large. *Journal of Petrology* **64**, 1–28.

Ziberna, L., Klemme, S. & Nimis, P. (2013). Garnet and spinel in fertile and depleted mantle: Insights from thermodynamic modelling. *Contributions to Mineralogy and Petrology* **166**, 411–421.

Figure captions

Figure 1 – Schematic view of (a) the East African Rift System (EARS), (b) the Virunga Volcanic Province (VVP), and the lava plain Nyiragongo, as based on the work of Thonnard and Denaeyer (1965) and Smets and Poppe (2016). Relevant volcanic provinces are indicated in (a) with red rectangles, among which is the VVP and its eight volcanic edifices Nyamulagira (Nyam), Nyiragongo (Nyir), Mikeno (Mik), Karasimbi (Kar), Visoke (Vis), Sabinyo (Sab), Gahinga (Gah), and Muhavura (Muh), as well as the Mugogo cone. Map (c) displays the broad topographical structure of the main edifice and its pyroclastic cones. Sampled cones have been indicated by colour and name. Samples associated with each cone are listed in Table 1.

Figure 2 – Main compositional diagrams of Nyiragongo lithologies. The TAS diagram after Le Bas *et al.* (1986) shown in (a) displays alkali-enrichment and silica-undersaturation. The primitive-mantle normalized (Sun and McDonough, 1989) multi-element variation diagram in (b) shows strong enrichment in LILE and LREE. Highlighted samples are those found in Table 1, whereas background literature data is derived from the compilation of Barette *et al.* (2017), the data of Minissale *et al.* (2019, 2022), and Molendijk *et al.* (2024). Abbreviations for samples types are moB (micro-olivine basalts), OCB (olivine-cpx basalts), OMB (olivine-melilite basalts), PMB (picritic melilite basalts), and P (picrites).

Figure 3 – Petrographic images in single- and cross-polarized light of (a) moB-type, (b) OMB-type, (c) PMB-type, and (d) P-type thin sections. Petrographically, CMB-types are near-identical to OMB-types, which is why this sample type is not displayed. Mineral abbreviations are for olivine (Ol), clinopyroxene (Cpx), and melilite (Mll).

Figure 4 – Distribution of analysed crystals per (a) olivine forsterite content and (b) spinel Cr# contents as listed per sample type.

Figure 5 – Olivine compositional diagrams correlating forsterite content with (a) Ni, (b) Ca, and (c) Mn contents. Fields of literature data are provided for olivine from Afar (Wong *et al.*, 2022), the Boku Volcanic Province (BVC) (Wong *et al.*, 2022), carbonatites from the Kola alkaline province (Vozniak *et al.*, 2023), the Tuscany alkaline province (Ammannati *et al.*, 2016; Bracco *et al.*, 2023), Uganda (Foley *et al.*, 2011), and the compilation for MORB data by Sobolev *et al.* (2007).

Figure 6 – Calculated crystallization temperatures for primitive olivine based on Cr-spinel Al-exchange equilibria following the model of Zhang *et al.* (2023). Crystallization temperature

ranges are included for a variety of other systems, as reported by the same study. Error bars on individual datapoints reflect the root-mean-square errors of the applied thermometers.

Figure 7 – Diagrams illustrating the involvement of mantle source components based on (a-c) whole-rock and (d-f) olivine compositions. Phlogopite is primarily indicated by low K/Rb ratios in (a). Both phlogopite and amphibole involvement can be inferred through Rb/Sr and Ba/Rb ratios in (b). Apatite involvement is indicated in high Th/U (a) and strong correlations between LREE and P_2O_5 (c). Olivine transition element ratios in (d) are indicative of a peridotite restite, whereas (e) Cr and (f) Ti concentrations indicate a lack of clear Cr-spinel or subduction recycling signatures. References for olivine compositions are the same as used in Fig. 5. Mineral compositions are derived from O'Reilly and Griffin (2000), Coltorti *et al.* (2007), Koornneef *et al.* (2009). Primitive mantle compositions are derived from Sun and McDonough (1989).

Figure 8 – Select diagrams showing melt compositional evolution with increasing melt degree (F) for modelling at 1 and 3 GPa, starting with the assemblages listed in Table 4. Notations 70 and 74 refer to assemblages being the best compositional matches for samples Mg_70 and Mg_74, respectively. Diamonds (1 GPa) and stars (3 GPa) indicate the best-fit point where the overall simulated melt composition best matches the target composition, as reported in Table 4. Grt-out, Phl-out, and Amp-out lines are displayed in relevant diagrams, indicated the complete consumption of garnet, phlogopite, and amphibole, respectively.

Figure 9 – Not to scale conceptual model for the lithosphere underlying the Nyiragongo volcano, including a schematic melting regime, preferentially melting phlogopite, garnet, and apatite bearing pyroxenite veins after which melts pond and ascend within the greater, olivine-dominated mantle. Scheme of the upper volcanic edifice is based on the work of Molendijk *et al.* (2024). The kink in the magmatic conduit represents a skip between lower and deeper zones for illustration purposes.

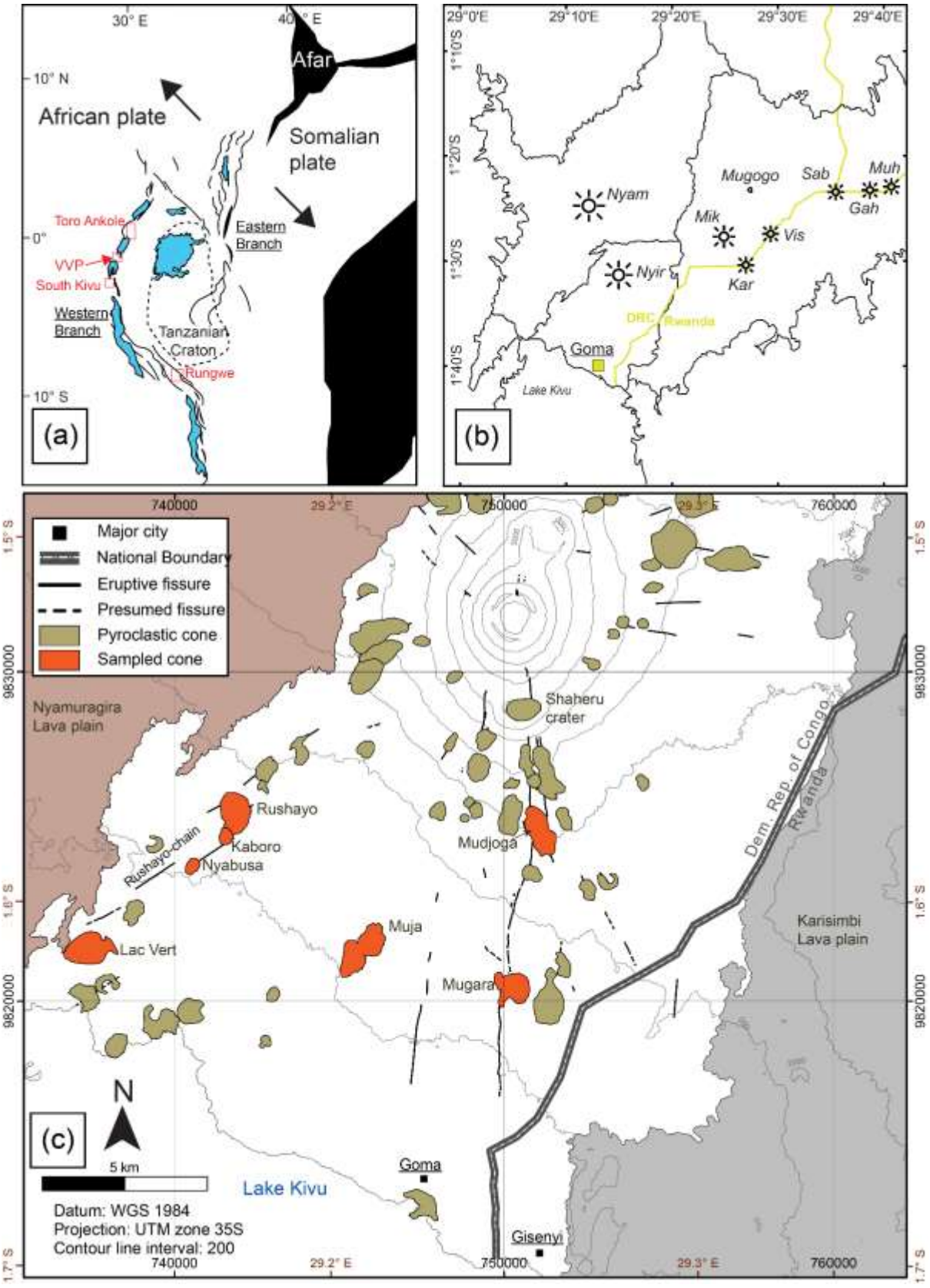
30° E
40° E
Afar
10° N
African plate
Somalian plate
Toro Ankole
0°
VVP
South Kivu
Western Branch
Eastern Branch
Tanzanian Craton
Rungwe
10° S
(a)
29°0'E
29°10'E
29°20'E
29°30'E
29°40'E
1°10'S
1°20'S
1°30'S
1°40'S
Nyam
Mugogo
Sab
Muh
Gah
Mik
Vis
Nyir
Kar
DRC
Rwanda
Goma
Lake Kivu
(b)
740000
29.2° E
750000
29.3° E
760000
1.5° S
1.6° S
1.7° S
9830000
9820000
Major city
National Boundary
Eruptive fissure
Presumed fissure
Pyroclastic cone
Sampled cone
Nyamuragira Lava plain
Shaheru crater
Rushayo
Kaboro
Nyabusa
Rushayo-chain
Mudjoga
Dem. Rep. of Congo
Rwanda
Muja
Lac Vert
Mugara
Karisimbi Lava plain
N
(c)
5 km
Lake Kivu
Goma
Gisenyi
Datum: WGS 1984
Projection: UTM zone 35S
Contour line interval: 200

Figure 1

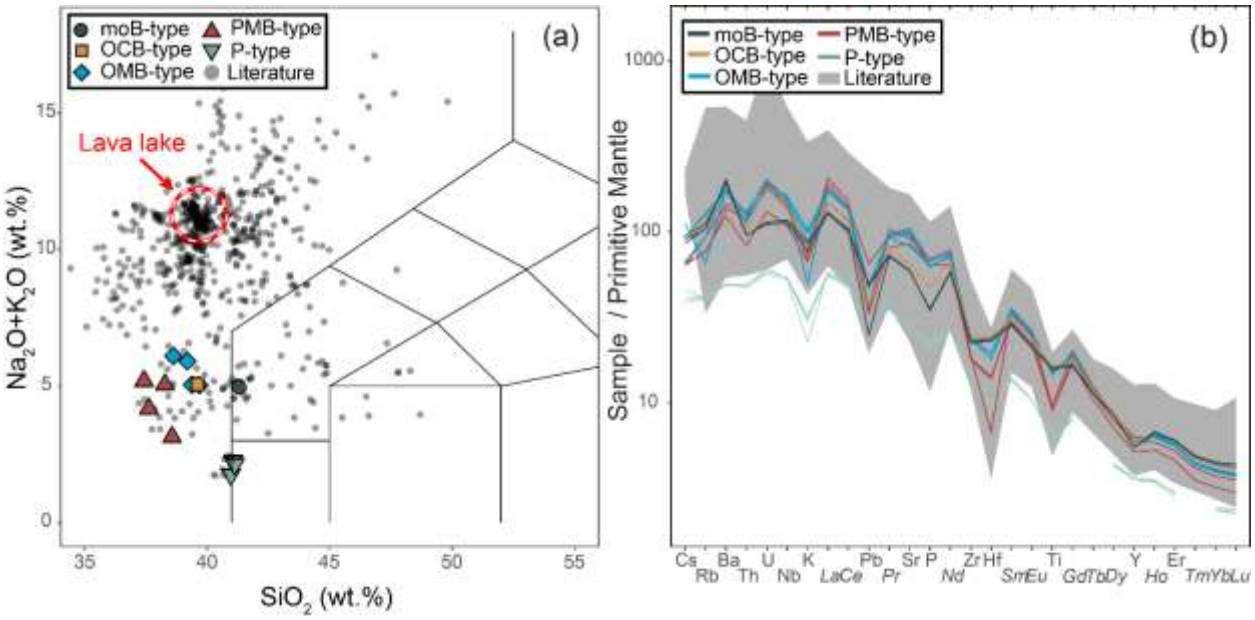

1168

1169 Figure 2

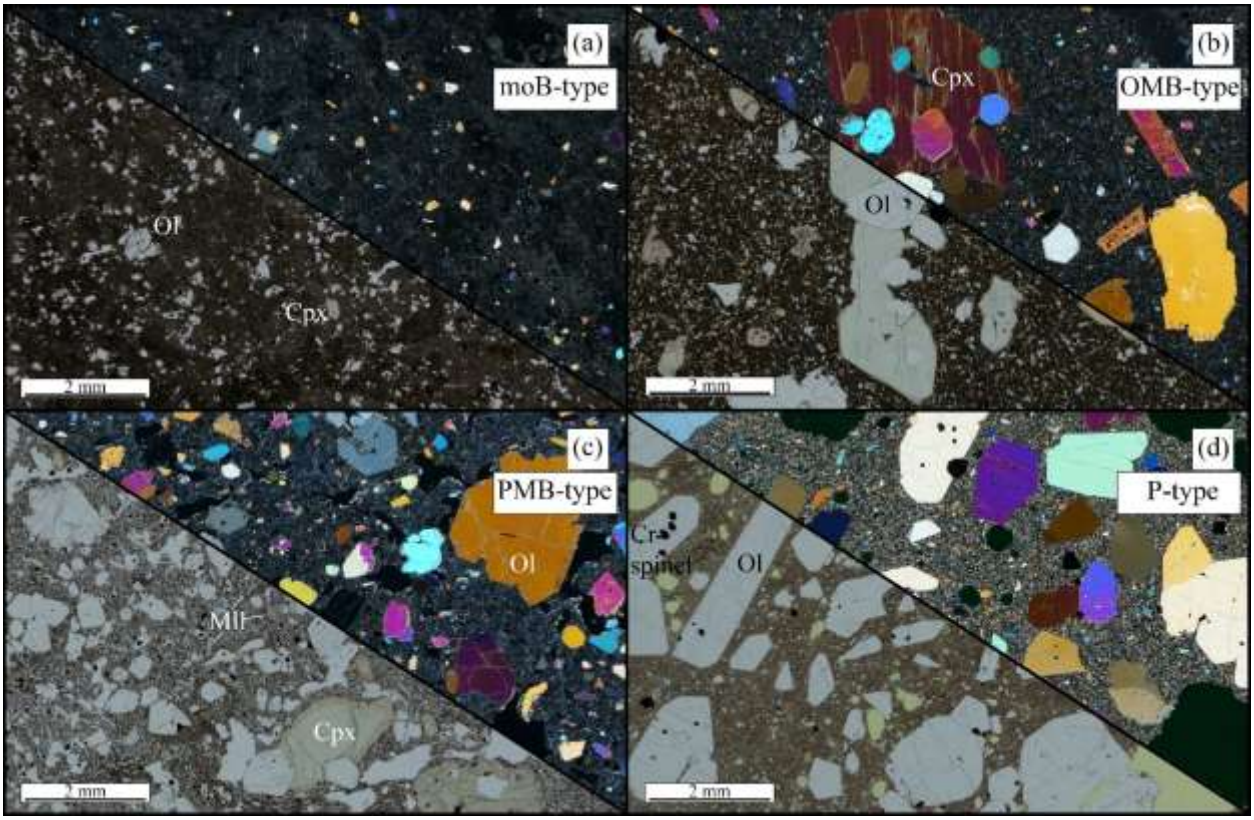
(a)
moB-type
Ol
Cpx
2 mm
(b)
OMB-type
Cpx
Ol
2 mm
(c)
PMB-type
Ol
Mlt
Cpx
2 mm
(d)
P-type
Cr-spinel
Ol
2 mm

Figure 3

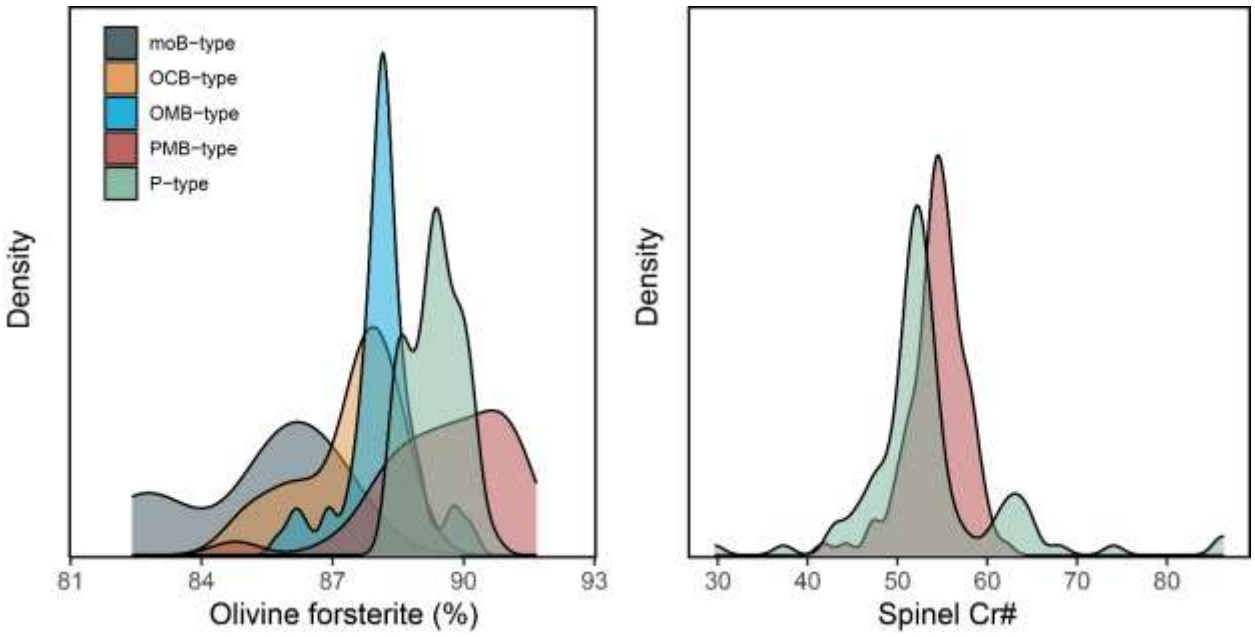

1172

1173 Figure 4

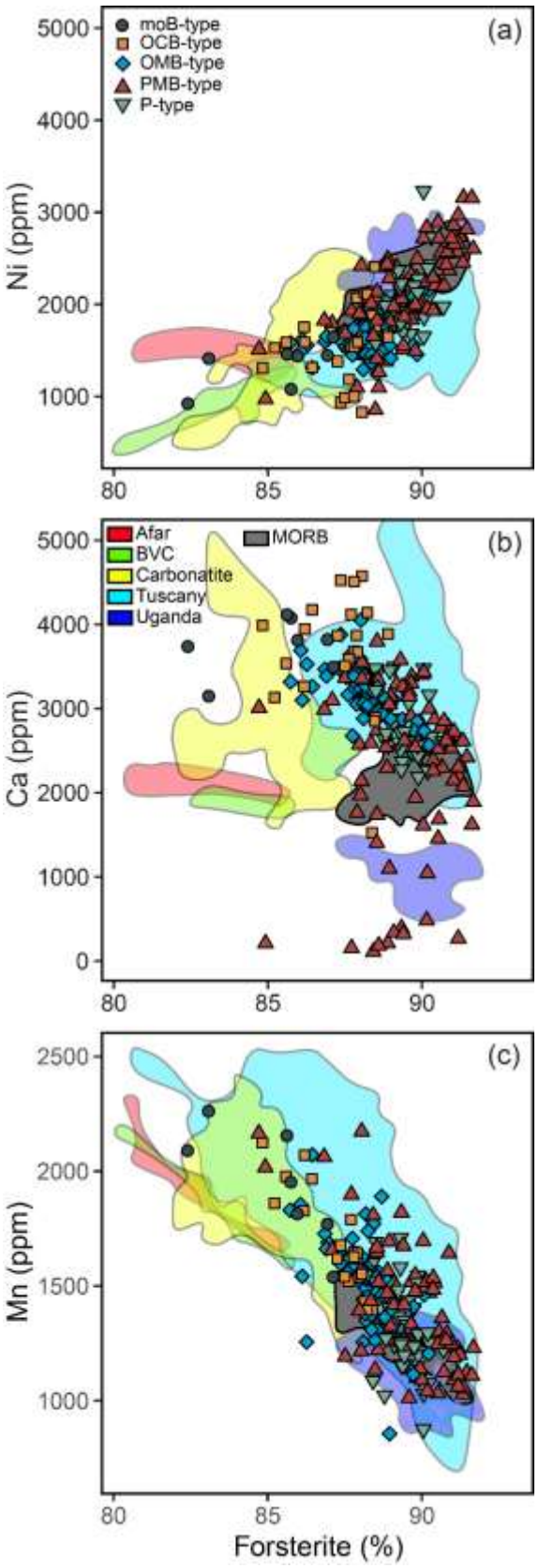

1174

1175 Figure 5

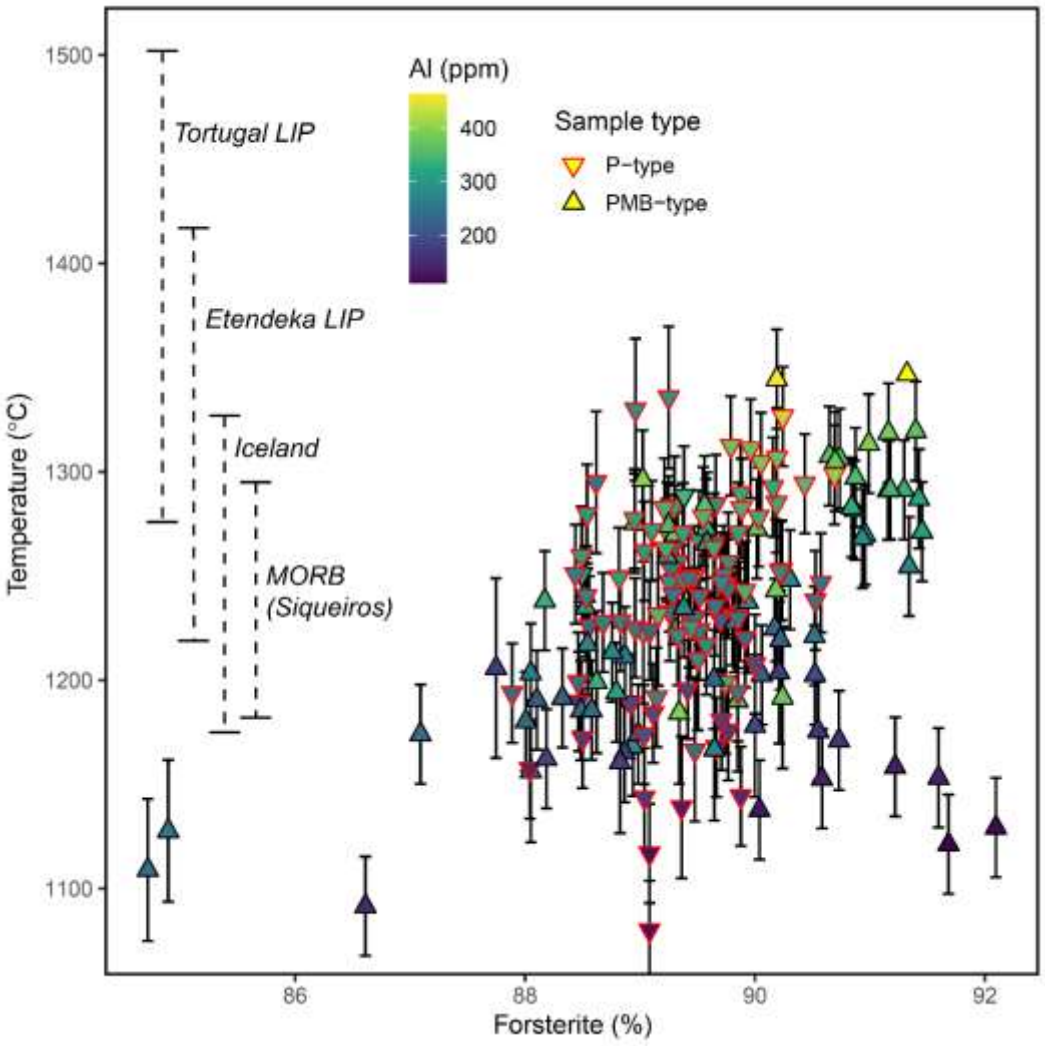

1176

1177 Figure 6

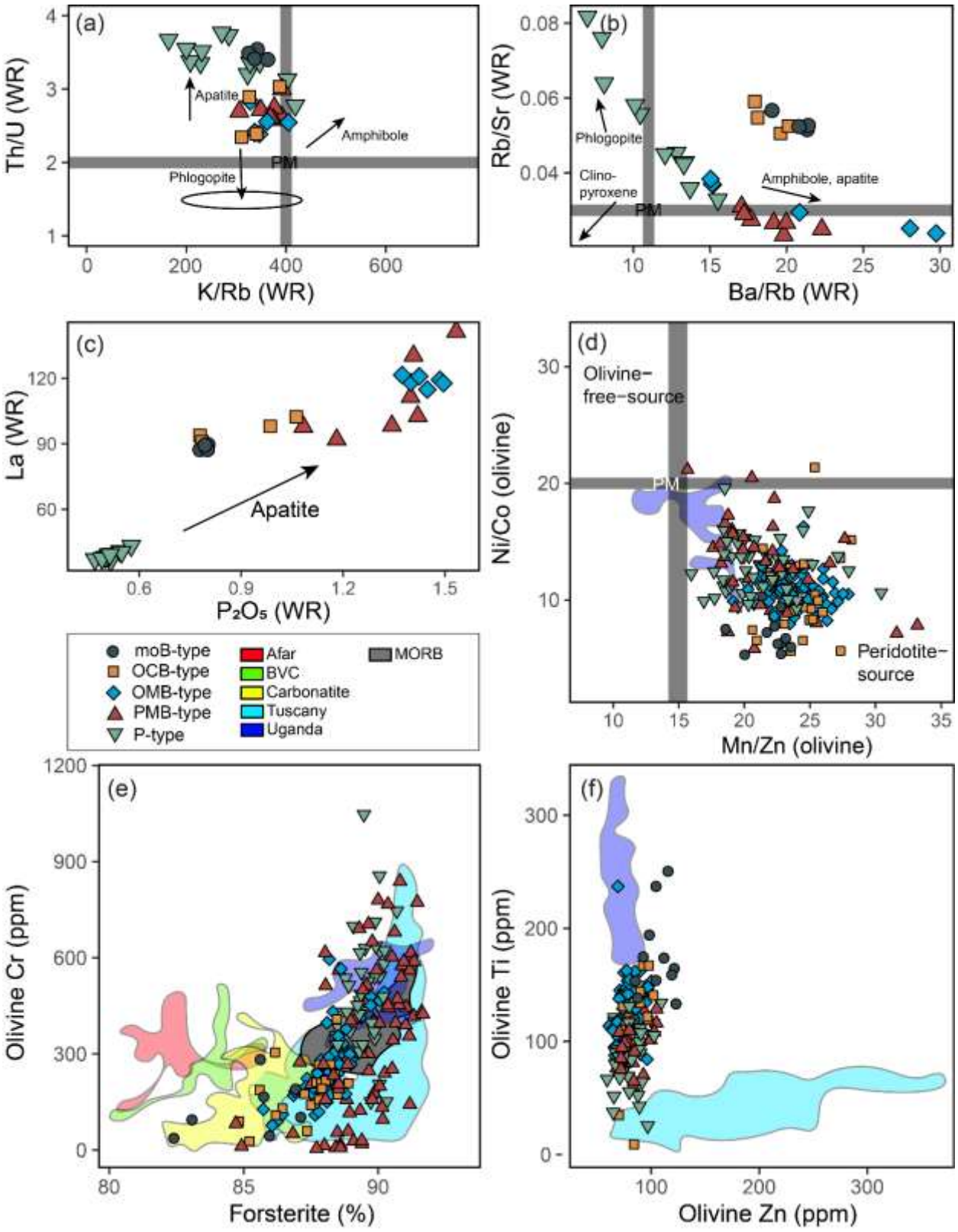

1178

1179 Figure 7

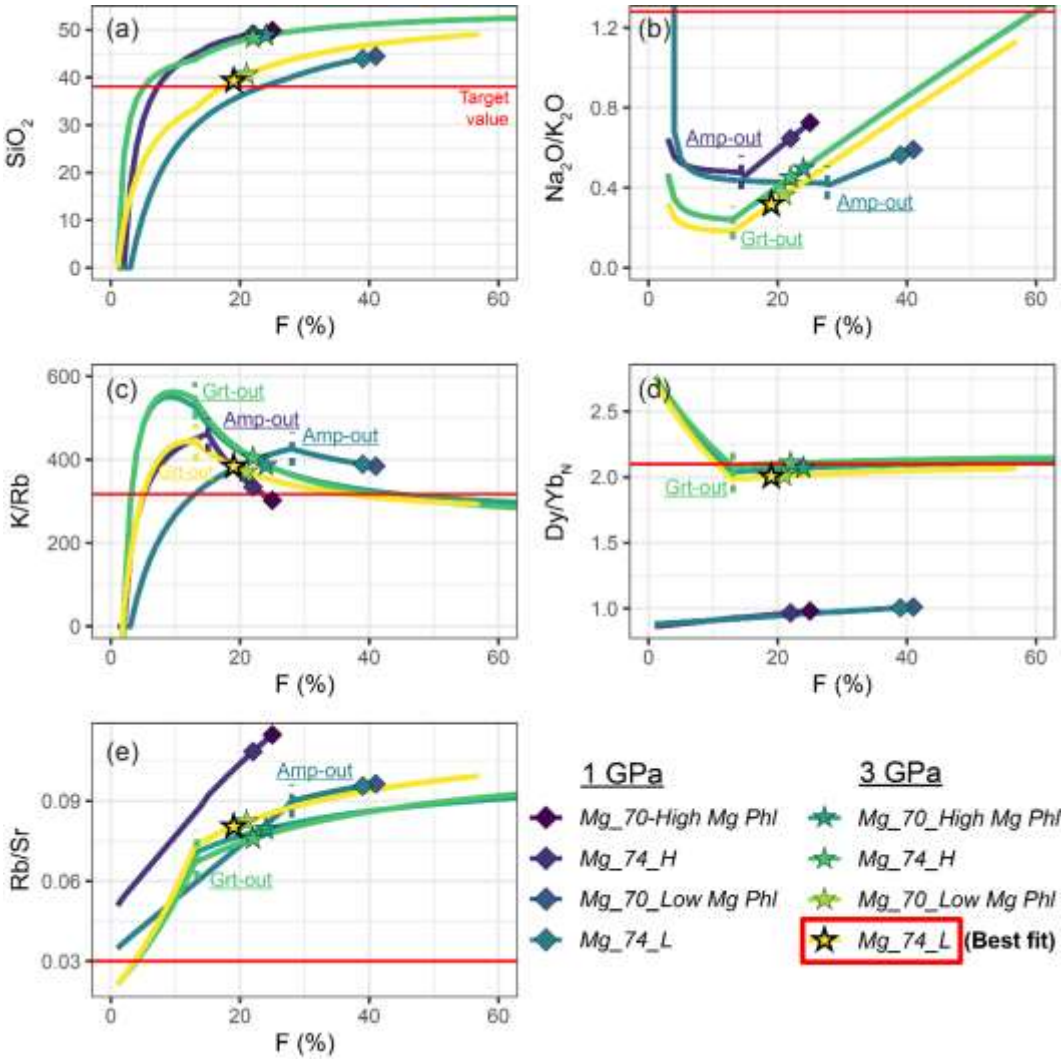

1180

1181 Figure 8

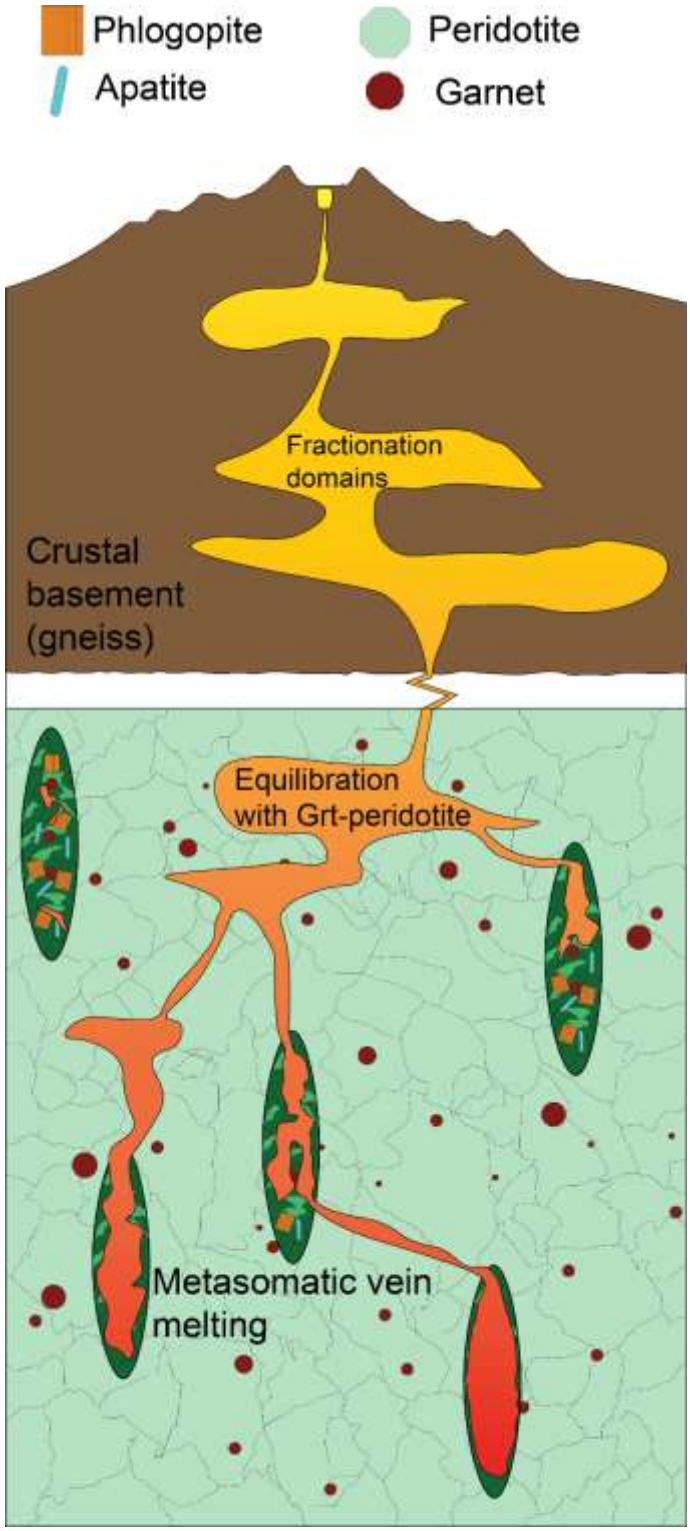
Phlogopite
Peridotite
Apatite
Garnet
Fractionation domains
Crustal basement (gneiss)
Equilibration with Grt-peridotite
Metasomatic vein melting

Figure 9